Computer Methods in Applied Mechanics and Engineering 462 (2026) 119246

Contents lists available at ScienceDirect

Comput. Methods Appl. Mech. Engrg.

journal homepage: www.elsevier.com/locate/cma

Thermodynamic regularization based computational framework for strain-induced crystallization

Mahmood Jabareen [b,d,1,*], Vu Nguyen-Xuân [a], Mikhail Itskov [a], Jean-Benoît Le Cam [c], Vu Ngoc Khiêm [a,*]

[a] Department of Continuum Mechanics, RWTH Aachen University, Eilfschornsteinstr. 18, 52062 Aachen, Germany
[b] Technion Israel Institute of Technology, Faculty of Civil and Environmental Engineering, Technion City, Haifa 3200003, Israel
[c] Université de Rennes, CNRS, IPR (Institut de Physique de Rennes) - UMR 6251, F-35000 Rennes, France
[d] ETH Zurich, Department of Mechanical and Process Engineering, Institute for Mechanical Systems, Zurich, Switzerland

ARTICLE INFO

Dataset link: https://doi.org/10.5281/zenodo.21356943

Keywords:
Thermodynamic regularization
Analytical inelasticity
Single potential formulation
Natural rubbers
Strain-induced crystallization
Loss of ellipticity

ABSTRACT

Strain-induced crystallization is a type of phase transition in natural rubbers triggered by deformation. The computation of this phenomenon necessitates proper numerical regularization due to the loss of ellipticity at the onset of strain-induced crystallization. This challenge is intensified by the absence of internal dissipation in such thermodynamic irreversible process, which precludes the use of dissipation potentials commonly employed in the literature. In this paper, we extend the recently developed thermodynamic regularization technique (i.e., regularization on the basis of thermodynamics of internal variables) to the case of natural rubbers, and formulate a novel computational framework for strain-induced crystallization which exhibits no internal dissipation. The computational framework coupling four fields (displacement, temperature and two nonlocal interactions) is then demonstrated through multiple numerical benchmarks and comparison with experimental data.

1. Introduction

The transformation of amorphous polymer chains into ordered molecular structures under deformation, known as strain-induced crystallization (SIC), plays a critical role in understanding the resistance of natural rubber to crack propagation [1]. However, the exothermic nature of this phase transition [2–4] results in complex behavior of natural rubber under varying loading conditions. To minimize the need for time-consuming and costly physical tests on natural rubber components, a robust computational framework capable of predicting the long-term performance of natural rubbers is desired.

Computation of SIC in natural rubbers is challenging due to the necessity of a comprehensive understanding of the thermodynamics of multiple fields, including deformation, temperature, and nonlocal interactions. Furthermore, it requires the integration of domain knowledge in numerical regularization, thermodynamics of internal variables and fundamental continuum mechanics. Indeed, to date most constitutive formulations [5–14] have not accounted for the zero internal dissipation observed in calorimetric measurements [15] of unfilled natural rubbers (see [16,17] as exceptions). Additionally, the loss of ellipticity at the onset of deformation-induced phase transition, as highlighted by Ericksen [18], has not been addressed. Accordingly, multiple equilibrium configurations may arise in a force-controlled experiment involving an elastic bar undergoing phase transition. These configurations

* Corresponding authors.
E-mail addresses: cvjmah@technion.ac.il (M. Jabareen), khiem.vu@rwth-aachen.de (V.N. Khiêm).
[1] On sabbatical leave from Technion – Israel Institute of Technology, Haifa, Israel.

https://doi.org/10.1016/j.cma.2026.119246
Received 12 April 2026; Received in revised form 15 July 2026; Accepted 16 July 2026
Available online 19 August 2026
0045-7825/© 2026 The Authors. Published by Elsevier B.V. This is an open access article under the CC BY license (http://creativecommons.org/licenses/by/4.0/).

result from strain discontinuities at phase boundaries as observed e.g. through scanning electron microscopy [19,20] or infrared thermography [21].

While the general concept of mathematical regularization for phase transitions is established, its physical foundation remains unclear. It is well known that the introduction of strain-like gradient terms can penalize the formation of regions with sudden spatial variations in strain [22–36]; however, arbitrary nonlocal formulations do not adhere to thermodynamic principles. For instance, the dissipation pseudo-potential approach [37] and the standard gradient damage formulation [26] are inadequate for unfilled natural rubbers due to the lack of internal dissipation during the irreversible thermodynamics of SIC, as evidenced by calorimetric measurements [15] and proven mathematically by [16].

In contrast, a thermodynamically based regularization technique known as thermodynamic regularization has been established [38]. Unlike previous methods, this approach does not fixate on a specific regularization formulation but instead adheres to the first principles of continuum mechanics, specifically the laws of thermodynamics and a single thermodynamic potential (i.e., the Helmholtz free energy). This renders it applicable across a broad spectrum of materials furnishing distinct thermodynamic behaviors while ensuring the physical interpretability of parameters and results. For instance, the technique has been successfully applied to textile reinforcements that exhibit strictly positive internal dissipation due to fiber sliding [38]. In such context, the regularization parameter corresponds to the bending stiffness of the fiber.

In the current work, we extend the thermodynamic regularization theory to the case of deformation-induced phase transition in unfilled natural rubbers. Our goals are twofold: (1) establish a physically-based regularization formulation for SIC in natural rubbers and (2) expand the theory of thermodynamic regularization. The paper is organized as follows. Section 2 introduces the local model for SIC. Section 3 discusses the loss of ellipticity that arises after the onset of crystallization. This issue is resolved using the thermodynamic regularization technique presented in Section 4, in which no internal dissipation occurs. Sections 5 and 6 present the finite-element framework for the resulting nonlocal theory. Finally, Section 7 provides detailed experimental data analyses and numerical benchmarks demonstrating the applicability of the proposed framework. Several Appendices introducing the calorimetric analysis of crystallizing polymers, relevant derivatives of crystallinities, and the derivation of the geometrical stiffness matrix are included.

2. Local Helmholtz free energy of natural rubbers

In this section, we summarize the main results of the constitutive formulation for crystallizing rubbers proposed by [16], since it is capable of explaining all the major effects of SIC aligning with the calorimetric experimental observations.

2.1. Kinetics of SIC

Polymer crystallites are ordered solid-like regions within a polymer network, formed by the aggregation of aligned neighboring polymer segments. In general, they can be induced by temperature or deformation. In the present paper, we are solely interested in strain-induced crystallites. The percentage of polymer segments in a polymer network involved in the solid state (crystallite) is denoted by the degree of crystallization (the so-called crystallinity). It is evaluated by the ratio between the crystalline reflection intensity and the total intensity (of both crystalline and amorphous phases) in X-ray diffraction measurements (see, e.g. [39]). The kinetics of crystallization generally refers to the time-dependent processes of nucleation and crystal growth. Since the current study focuses exclusively on rate-independent SIC, the kinetics of crystallization is considered equivalent to the evolution of crystallinity with respect to deformation. It should be noted that the crystallinity in this context is not treated as an internal variable.

According to [16], there are two families of crystallites with different morphologies forming in loading and unloading conditions of natural rubbers. They are referred to as primary and secondary crystallites, respectively. Therefore, total crystallinity is additively decomposed into primary and secondary crystallites and it is given by

$$\zeta = \zeta_{\mathrm{I}} + \zeta_{\mathrm{II}}. \tag{1}$$

In particular, the primary crystallites can form in any direction within a unit sphere at the continuum material point

$$\zeta_{\mathrm{I}} = B_1 \exp\left(-\frac{\Delta G^*\left(\varepsilon_1, \varepsilon_2\right)}{k_{\mathrm{B}} T_0}\right), \tag{2}$$

where B_1 is the primary crystallinity constant, k_{B} is the Boltzmann constant, and T_0 is the initial temperature. Also, ε_1 and ε_2 are the maximum and middle principal strains, respectively. The energy barrier for crystal nucleation $\Delta G^*\left(\varepsilon_1, \varepsilon_2\right)$ is given by

$$\Delta G^*\left(\varepsilon_1, \varepsilon_2\right) = \frac{8\pi\gamma_t\gamma_s^2}{\Delta\Psi^2\left(\varepsilon_1, \varepsilon_2\right)}, \tag{3}$$

where γ_t and γ_s are the surface tensions at the top and on the side of a primary crystallite, respectively. The change in the free energy $\Delta\Psi$ of the oriented network strands is given by

$$\Delta\Psi\left(\varepsilon_1, \varepsilon_2\right) = w_{\mathrm{L}} \frac{N_{\mathrm{c0}}}{3} k_{\mathrm{B}} T_0 \kappa n \left[\ln\left(\frac{\sin\frac{\pi}{\sqrt{n}}\cdot\left(\varepsilon_1+1\right)}{\sin\left(\frac{\pi}{\sqrt{n}}\left(\varepsilon_1+1\right)\right)}\right) - \ln\left(\frac{\sin\frac{\pi}{\sqrt{n}}\cdot\left(\varepsilon_2+1\right)}{\sin\left(\frac{\pi}{\sqrt{n}}\left(\varepsilon_2+1\right)\right)}\right)\right], \tag{4}$$

where n is the average number of chain segments in the representative chain. N_{c0} is the initial number of chains in natural rubber, and $w_{\mathrm{L}} = 0.3$ denotes the limit fraction of chain alignment.

Remark 1. Eq. (4) takes into account the influence of biaxiality on SIC in unfilled natural rubber. In equibiaxial tension, the nucleation barrier is infinite, indicating that the strain-induced crystallinity of unfilled natural rubbers is zero under equibiaxial tension as the polymer chains are too widely separated to form bundle-like crystallites. In the special case of uniaxial tension, the second term in (4) is negligible, so that $\Delta\Psi = w_{\mathrm{L}}\frac{N_{\mathrm{c0}}}{3}k_{\mathrm{B}}T_0\kappa n\ln\left(\frac{\sin\frac{\pi}{\sqrt{n}}\cdot(\varepsilon_1+1)}{\sin\left(\frac{\pi}{\sqrt{n}}(\varepsilon_1+1)\right)}\right)$, this model reproduces the previous theoretical description of SIC in uniaxial tension [16].

Furthermore, secondary crystallites form in any unloading direction (i.e., with $\dot{\varepsilon}_i \le 0$) by diffusion of chain segments into existing nuclei (primary crystallites) in the polymer network [16]. The secondary crystallinity can be given by

$$\zeta_{\mathrm{II}} = \sum_{i=1}^{2} B_2 \exp\left(-\frac{\Delta\overline{G}^{*}\left(\varepsilon_i\right)}{k_{\mathrm{B}}T_0}\right)\left[\exp\left(-\frac{\Delta\widehat{G}^{*}\left(\Lambda_i^{\mathrm{c\,max}}-1\right)}{k_{\mathrm{B}}T_0}\right)-\exp\left(-\frac{\Delta\widehat{G}^{*}\left(\varepsilon_i\right)}{k_{\mathrm{B}}T_0}\right)\right], \tag{5}$$

where B_2 is the secondary crystallinity constant. The energy barriers $\Delta\overline{G}^{*}$ and $\Delta\widehat{G}^{*}$ for the formation and melting of secondary crystallites are, respectively, defined by

$$\Delta\overline{G}^{*}\left(\varepsilon_i\right) = \frac{8\pi\overline{\gamma}_t\overline{\gamma}_s^{2}}{\Psi_i^{2}\left(\varepsilon_i\right)}, \quad \Delta\widehat{G}^{*}\left(\varepsilon_i\right) = \frac{8\pi\widehat{\gamma}_t\widehat{\gamma}_s^{2}}{\Psi_i^{2}\left(\varepsilon_i\right)}, \quad i=1,2, \tag{6}$$

where the new surface tension products $\overline{\gamma}_t\overline{\gamma}_s^{2}$ and $\widehat{\gamma}_t\widehat{\gamma}_s^{2}$ are used since the morphology of the secondary crystallites is different from that of the primary crystallite. To be consistent with [16], we set $\overline{\gamma}_t\overline{\gamma}_s^{2} = \frac{\gamma_t\gamma_s^{2}}{\overline{\chi}^{2}}$ and $\widehat{\gamma}_t\widehat{\gamma}_s^{2} = \frac{\gamma_t\gamma_s^{2}}{\widehat{\chi}^{2}}$, where $\overline{\chi}$ and $\widehat{\chi}$ represent the relative ratio of surface tension for secondary formation and secondary melting, respectively. Therein, the relative ratio of the surface tension for secondary formation $\overline{\chi} > 1$ indicates that it is easier to form secondary crystallites than primary ones due to the availability of nuclei in unloading. Furthermore, the free energy Ψ_i of each network strand is given by

$$\Psi_i\left(\varepsilon_i\right) = w_{\mathrm{L}}\frac{N_{\mathrm{c0}}}{3}k_{\mathrm{B}}T_0\kappa n\ln\left(\frac{\sin\frac{\pi}{\sqrt{n}}\cdot\left(\varepsilon_i+1\right)}{\sin\left(\frac{\pi}{\sqrt{n}}\left(\varepsilon_i+1\right)\right)}\right), \quad i=1,2. \tag{7}$$

For the diffusion of chain segments into the secondary crystallites [16], internal variables associated with the maximal cyclic stretches $\Lambda_i^{\mathrm{c\,max}}$ are introduced and they are defined as

$$\Lambda_i^{\mathrm{c\,max}} = \max_{\tau\in\left[t_i^{\mathrm{c}},t\right]}\Lambda_i\left(\tau\right), \quad i=1,2, \tag{8}$$

where Λ_1 and Λ_2 are the maximum and middle principal stretches, respectively. The ending time of the closest directional loading cycle t_i^{c} is defined by the local minimum of Λ_i within the time interval $\tau\in(-\infty,t]$, $i=1,2$. According to (8), the maximal cyclic stretch $\Lambda_i^{\mathrm{c\,max}}$ coincides with the macroscale principal stretch Λ_i during the loading or reloading process $\dot{\Lambda}_i > 0$, while it remains constant (i.e. $\dot{\Lambda}_i^{\mathrm{c\,max}} = 0$) during the unloading process $\dot{\Lambda}_i < 0$. Finally, the scalar-valued internal variables in our model can be condensed into a tensor-valued internal variable as

$$\boldsymbol{\Xi} = \sum_{i=1}^{2}\Lambda_i^{\mathrm{c\,max}}\boldsymbol{M}_i\otimes\boldsymbol{M}_i, \tag{9}$$

where $\boldsymbol{M}_1$ and $\boldsymbol{M}_2$ are the eigenvectors of $\mathbf{C}$ corresponding to the maximum and middle principal stretches. It should be noted that

$$\frac{\partial\zeta_{\mathrm{II}}}{\partial\boldsymbol{\Xi}} : \dot{\boldsymbol{\Xi}} = 0, \tag{10}$$

since $\zeta_{\mathrm{II}} \equiv 0$ under loading while $\dot{\Lambda}_i^{\mathrm{c\,max}} = 0$ under unloading.

2.2. Local internal energy of natural rubbers

The local internal energy of natural rubber can be additively decomposed by [16]

$$U\left(\mathbf{F},T,\boldsymbol{\Xi}\right) = U_{\mathbf{F}}\left(\mathbf{F},\boldsymbol{\Xi}\right) + U_{\theta}\left(T\right). \tag{11}$$

The deformation-dependent part of internal energy $U_{\mathbf{F}}$ will be discussed later. The second term $U_{\theta}(T)$ due to the raise of temperature is given by

$$U_{\theta}\left(T\right) = c_0\left(T-T_0\right), \tag{12}$$

where c_0 denotes the heat capacity per unit reference volume of natural rubber and T is the absolute temperature.

2.3. Local entropy of natural rubbers

According to [16], the entropy of a natural rubber network is given by

$$\begin{aligned}\eta(\mathbf{F},T,\Xi) &= \eta_{\mathbf{F}}(\mathbf{F},\Xi)+\eta_{\theta}(T)\\ &= N_{\mathrm{c}}(\mathbf{F},\Xi)\, s_{\mathbf{F}}(\mathbf{F})+\eta_{\theta}(T),\end{aligned} \tag{13}$$

where $\eta_{\mathbf{F}}(\mathbf{F},\Xi)$ and $\eta_{\theta}(T)$ are the deformation-dependent and temperature-dependent entropies of the network, respectively. $N_{\mathrm{c}}(\mathbf{F},\Xi)$ denotes the effective number of chains per unit reference volume, and $s_{\mathbf{F}}(\mathbf{F})$ is the deformation-dependent entropy of a single chain. Specifically, the individual entropy can be obtained from a tube model in polymer physics as follows [16]

$$s_{\mathbf{F}}(\mathbf{F}) = -k_{\mathrm{B}} n\kappa \ln \frac{\frac{\pi}{n} r(\mathbf{F})}{\sin\left(\frac{\pi}{n} r(\mathbf{F})\right)} - k_{\mathrm{B}}\omega\upsilon(\mathbf{F}), \tag{14}$$

where ω is a geometric parameter of the tube. The constant $\kappa = \frac{9}{\pi^2}$ results from the spring constant of the linear coarse-grained model [40], while the end-to-end distance of semi-crystalline chain $r(\mathbf{F})$ is given by

$$r(\mathbf{F}) = \lambda(\mathbf{F})\sqrt{n} - \zeta_{\mathrm{I}}\left(\varepsilon_1(\mathbf{F}),\varepsilon_2(\mathbf{F})\right) n_{\mathrm{c}}, \tag{15}$$

where $n_{\mathrm{c}} = 8n/9$ represents the number of molecular monomers involved in the chain alignments. The microscopic kinematic deformation measures (i.e. $\lambda(\mathbf{F})$ and $\upsilon(\mathbf{F})$) are linked with the macroscopic deformation gradient $\mathbf{F}$ via a two-step transition. First, the scale bridging between macroscale (at a continuum material point) and mesoscale (at the representative strand) is made by analytical homogenization [16,40–42]. Afterward, the microscopic stretch (of the representative chain) is related to the mesoscopic stretch by a stretch amplification. Specifically, microscopic kinematic deformation measures are given by [16,40]

$$\lambda(\mathbf{F}) = \left(\sqrt{\frac{I_1(\mathbf{F})}{3}}\right)^{q(\mathbf{F})}, \quad \upsilon(\mathbf{F}) = \sqrt{\frac{I_2(\mathbf{F})}{3}}, \tag{16}$$

where I_1 and I_2 denote the first and second principal invariants of the right Cauchy–Green tensor $\mathbf{C} = \mathbf{F}^{\mathrm{T}}\mathbf{F}$, respectively, and $q(\mathbf{F})$ is the stretch amplification exponent, which depends on the network inhomogeneity [16,40,42]. It can be expressed by

$$q(\mathbf{F}) = q_0\left(1+\zeta_{\mathrm{I}}\left(\varepsilon_1(\mathbf{F}),\varepsilon_2(\mathbf{F})\right)\right), \tag{17}$$

where q_0 is the initial stretch amplification exponent. Furthermore, due to the topological constraint, a polymer chain can only take part in the crystallization of either primary or secondary crystallite. Thus, the effective number of chains involved in the nucleation of the primary crystallite can be calculated as

$$N_{\mathrm{c}}(\mathbf{F},\Xi) = N_{\mathrm{c}0}\left(1-2\zeta_{\mathrm{II}}\left(\varepsilon_1(\mathbf{F}),\varepsilon_2(\mathbf{F}),\Xi\right)\right). \tag{18}$$

Because strain-induced crystallization saturates, the crystallinity cannot exceed 0.3 [43,44]. Therefore, $\zeta_{\mathrm{II}} < \zeta \leq 0.3$, which guarantees that the effective number of chains is always positive.

Finally, the temperature-dependent entropy of the rubber network is given by

$$\eta_{\theta}(T) = c_0 \ln\frac{T}{T_0}. \tag{19}$$

2.4. Local free energy of natural rubbers

In view of (11) and (13), the local free energy of natural rubbers can be expressed as

$$\Psi(\mathbf{F},T,\Xi) = U(\mathbf{F},T,\Xi) - T\eta(\mathbf{F},T,\Xi). \tag{20}$$

Note that $U_{\mathbf{F}} = 0$ in loading, and to simplify the stress formulation, we additionally require that [16]

$$\frac{\partial U_{\mathbf{F}}(\mathbf{F},\Xi)}{\partial\mathbf{F}} = T s_{\mathbf{F}}(\mathbf{F})\frac{\partial N_{\mathrm{c}}(\mathbf{F},\Xi)}{\partial\mathbf{F}}. \tag{21}$$

3. Loss of ellipticity after the onset of SIC

The onset of SIC occurs at a stretch where a diffraction of the X-rays or/and an additional heat production is detected. Generally speaking, this onset occurs at a stretch ratio of approximately 4 in unfilled natural rubber. During this process, the first elasticity tensor may, in some cases, become ill-posed, causing the governing equations to lose their ellipticity (i.e. loss of ellipticity). This is evident from the heterogeneities in temperature distribution observed in unfilled natural rubbers subjected to homogeneous uniaxial tension [21], as temperature variations in natural rubber are attributed to SIC. These heterogeneities become pronounced following the onset of SIC, particularly within the stretch ratio range of 4 to 5.5 (see Fig. 1). Interestingly, prior to the onset of SIC ($\Lambda_1 < 4$) and following the stress upturn ($\Lambda_1 \geq 6$), the temperature distribution remains homogeneous. This observation further implies that this behavior does not stem from coupling instabilities (see e.g. [45–48]), as observed in electroactive elastomers, but rather from the loss of ellipticity associated with phase transitions.

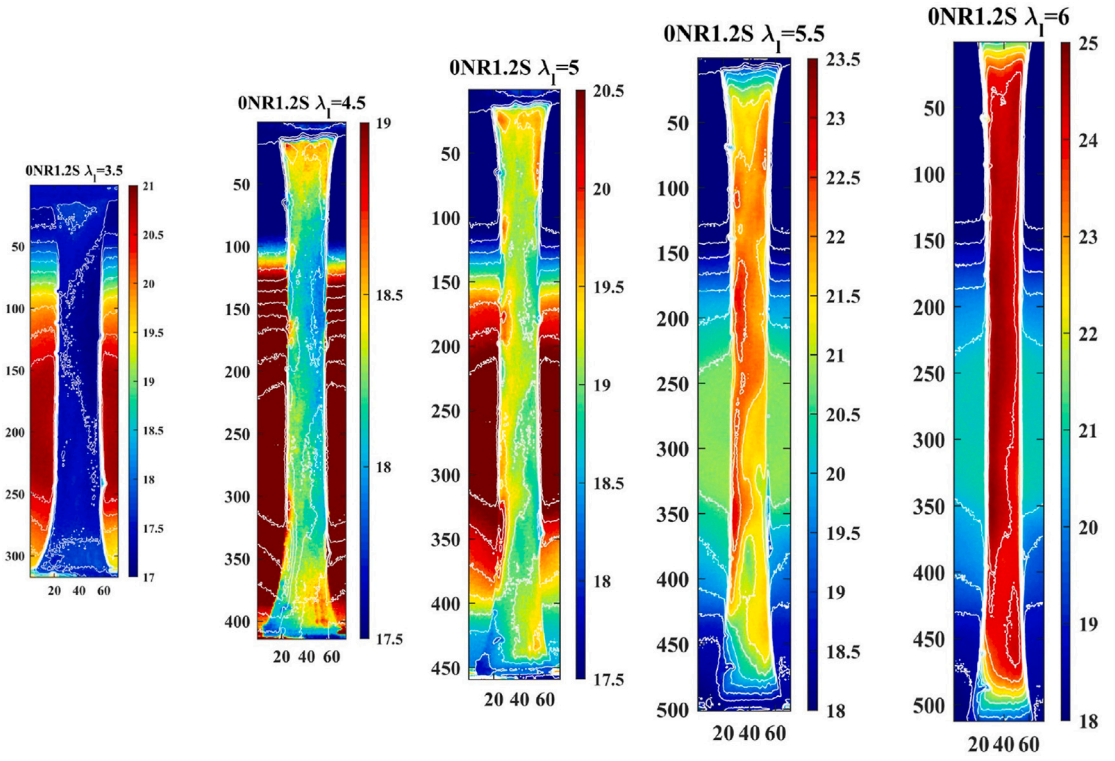


Fig. 1. Heterogeneity of temperature distribution after the onset of SIC ($\Lambda_1 = 4 - 5.5$) in a homogeneous uniaxial tension of unfilled natural rubber [21].

According to [49], the strong ellipticity condition (so-called the strict Legendre-Hadamard condition) requires that

$$e(\boldsymbol{v}, \boldsymbol{N}) = (\boldsymbol{v} \otimes \boldsymbol{N}) : \mathbb{A} : (\boldsymbol{v} \otimes \boldsymbol{N}) > 0, \quad \forall \boldsymbol{v}, \boldsymbol{N} \in \boldsymbol{E}^3 \tag{22}$$

where $\mathbb{A}$ is the first elasticity tensor, and $\boldsymbol{v}, \boldsymbol{N}$ denote arbitrary unit vectors. Specifically, the first elasticity tensor is defined by

$$\mathbb{A} = \frac{\partial \mathbf{P}}{\partial \mathbf{F}}, \tag{23}$$

where $\mathbf{P}$ is the first Piola–Kirchhoff stress tensor given by

$$\mathbf{P} = \frac{\partial \Psi}{\partial \mathbf{F}} - p\mathbf{F}^{-\mathrm{T}} = -N_c T \frac{\partial s_{\mathbf{F}}}{\partial \mathbf{F}} - p\mathbf{F}^{-\mathrm{T}}. \tag{24}$$

In (24), p is a Lagrange multiplier that enforces the incompressibility condition. We can write by (14), noting that the effective number of chains involved in the nucleation of the primary crystallite during the loading does not change (i.e. $N_c = N_{c0}$) and assuming that the temperature remains constant at the onset of strain induced crystallization (i.e. $T = T_0$),

$$\mathbf{P} = \mu_{c0} f_r \frac{\partial r}{\partial \mathbf{F}} + \mu_{t0} \frac{\partial \upsilon}{\partial \mathbf{F}} - p\mathbf{F}^{-\mathrm{T}}, \tag{25}$$

where the first derivatives of the end-to-end distance of semi-crystalline chain, the microscopic kinematic deformation measures, and primary crystallinity with respect to the deformation gradient are given by

$$\begin{aligned}
\frac{\partial r}{\partial \mathbf{F}} &= \sqrt{n} \frac{\partial \lambda}{\partial \mathbf{F}} - n_c \frac{\partial \zeta_1}{\partial \mathbf{F}}, \\
\frac{\partial \lambda}{\partial \mathbf{F}} &= q \frac{\lambda}{I_1} \mathbf{F} + \frac{q_0}{q} \lambda \ln(\lambda) \frac{\partial \zeta_1}{\partial \mathbf{F}}, \\
\frac{\partial \upsilon}{\partial \mathbf{F}} &= \frac{\upsilon}{I_2} \mathbf{F} \left(I_1 \mathbf{I} - \mathbf{C} \right), \\
\frac{\partial \zeta_1}{\partial \mathbf{F}} &= \sum_{i=1}^{2} \frac{1}{\Lambda_i} \frac{\partial \zeta_1}{\partial \epsilon_i} \mathbf{F} \left(\boldsymbol{M}_i \otimes \boldsymbol{M}_i \right),
\end{aligned} \tag{26}$$

and the auxiliary function f_r is defined by

$$f_r = \frac{n}{r} - \pi \cot\left(\frac{\pi}{n} r \right). \tag{27}$$

Table 1
Material constants of the local model for the natural rubber NR1.2 in [21].

μ_{c0} [MPa]	n	q_0	μ_{t0} [MPa]	B_1	B_2	$\gamma_t\gamma_s^2$ [$\frac{\text{mJ}^3}{\text{mm}^6}$]	$\check{\chi}$	$\hat{\chi}$	T_0 [K]	$\mathcal{K}$ [MPa]
0.1813	81	1.0373	0.6	0.32754	0.45301	$3.8432e^{-19}$	4.9565	1	293	$1e^4$

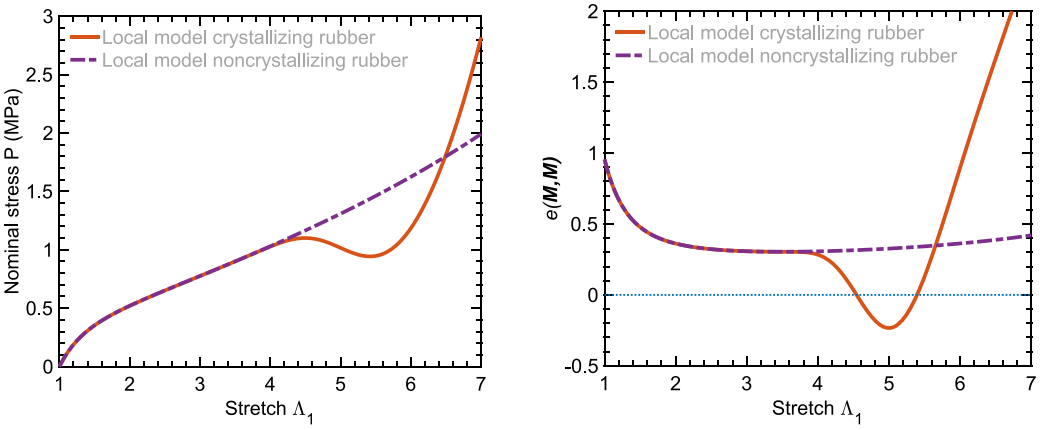


Fig. 2. Loss of ellipticity after the onset of SIC for crystallizing rubber undergoing uniaxial tension deformation: (a) stress–strain curve, and (b) the eigenvalue of the first elasticity tensor. Note that strong ellipticity is always observed in non-crystallizing rubber, and is evident in crystallizing rubber before the onset of crystallization and after the stress upturn.

Substituting (25), the first elasticity tensor becomes

$$\mathbb{A} = \mu_{c0} f_r \left(\sqrt{n} \frac{\partial^2 \lambda}{\partial \mathbf{F} \partial \mathbf{F}} - n_c \frac{\partial^2 \zeta_1}{\partial \mathbf{F} \partial \mathbf{F}} \right) + \mu_{c0} \frac{d f_r}{d r} \frac{\partial r}{\partial \mathbf{F}} \otimes \frac{\partial r}{\partial \mathbf{F}} + \mu_{t0} \frac{\partial^2 \upsilon}{\partial \mathbf{F} \partial \mathbf{F}} - p \frac{\partial \mathbf{F}^{-\mathrm{T}}}{\partial \mathbf{F}}, \tag{28}$$

where

$$\begin{aligned}
\frac{\partial^2 \lambda}{\partial \mathbf{F} \partial \mathbf{F}} &= q \frac{\lambda}{I_1} \mathbb{I} + q(q-2) \frac{\lambda}{I_1^2} \mathbf{F} \otimes \mathbf{F} + q_0 \frac{\lambda}{I_1} (\ln(\lambda) + 1) \left(\mathbf{F} \otimes \frac{\partial \zeta_1}{\partial \mathbf{F}} + \frac{\partial \zeta_1}{\partial \mathbf{F}} \otimes \mathbf{F} \right) + \frac{q_0}{q} \lambda \ln(\lambda) \frac{\partial^2 \zeta_1}{\partial \mathbf{F} \partial \mathbf{F}} + \frac{q_0^2}{q^2} \lambda \ln^2(\lambda) \frac{\partial \zeta_1}{\partial \mathbf{F}} \otimes \frac{\partial \zeta_1}{\partial \mathbf{F}}, \\
\frac{\partial^2 \upsilon}{\partial \mathbf{F} \partial \mathbf{F}} &= \frac{\upsilon}{I_2^2} (I_1 \mathbf{F} - \mathbf{F}\mathbf{C}) \otimes (I_1 \mathbf{F} - \mathbf{F}\mathbf{C}) + \frac{\upsilon}{I_2} \left(I_1 \mathbb{I} + 2 \mathbf{F} \otimes \mathbf{F} - \frac{\partial (\mathbf{F}\mathbf{C})}{\partial \mathbf{F}} \right), \\
\frac{\partial^2 \zeta_1}{\partial \mathbf{F} \partial \mathbf{F}} &= \sum_{i=1}^{2} \sum_{j=1}^{2} \left[\frac{1}{\Lambda_i \Lambda_j} \left(\frac{\partial^2 \zeta_1}{\partial \varepsilon_i \partial \varepsilon_j} - \frac{\delta_{ij}}{\Lambda_i} \frac{\partial \zeta_1}{\partial \varepsilon_i} \right) (\mathbf{F} \boldsymbol{M}_i \otimes \boldsymbol{M}_i) \otimes (\mathbf{F} \boldsymbol{M}_j \otimes \boldsymbol{M}_j) \right] + \sum_{i=1}^{2} \frac{1}{\Lambda_i} \frac{\partial}{\partial \varepsilon_i} \frac{\partial (\mathbf{F} \boldsymbol{M}_i \otimes \boldsymbol{M}_i)}{\partial \mathbf{F}},
\end{aligned} \tag{29}$$

and δ_{ij} denotes a Kronecker-Delta function. Fig. 2*a* shows the nominal axial stress versus the axial stretch, while Fig. 2*b* demonstrates the relation between the quantity $e(\boldsymbol{M}, \boldsymbol{M})$ and the macroscopic stretch using material parameters in Table 1 for the local model (20). The prediction for noncrystallizing rubber can be obtained using the same set of material constants, with the exception that $\gamma_t \gamma_s^2 \to \infty$. This condition implies that crystallization cannot occur in such material due to an infinite energy barrier via (3). It can be seen that the loss of ellipticity occurs after the onset of SIC in uniaxial tension of the crystallizing rubber, particularly within the stretch ratio range of 4.5–5.3 (cf. Fig. 2b). In contrast, no loss of ellipticity is observed for noncrystallizing rubber; or prior to the onset of SIC ($\Lambda_1 < 4$) and following the stress upturn ($\Lambda_1 \geq 6$) in crystallizing rubber (cf. Fig. 2). In other words, the phase transition in unfilled natural rubbers induces breakdown of ellipticity of the governing partial differential equations in this numerical example.

Remark 2. To the best of our knowledge, this is the first demonstration of the loss of ellipticity in strain-induced crystallizing polymers for three-dimensional loading scenario, i.e., the stress is a multivariate function in terms of the components of deformation gradient. Furthermore, the onset of loss of ellipticity is explicitly determined, rather than approximated in an asymptotic manner (cf. [50]), due to rigorous physical foundation of the model.

4. Thermodynamic regularization theory

As discussed in Section 3, ellipticity of the constitutive formulation fails at the onset of SIC. Ericksen [18] suggested that this issue is common in all materials undergoing phase transitions. To the best of our knowledge, a proper and thermodynamically meaningful numerical treatment for this problem has not yet been developed for natural rubbers.

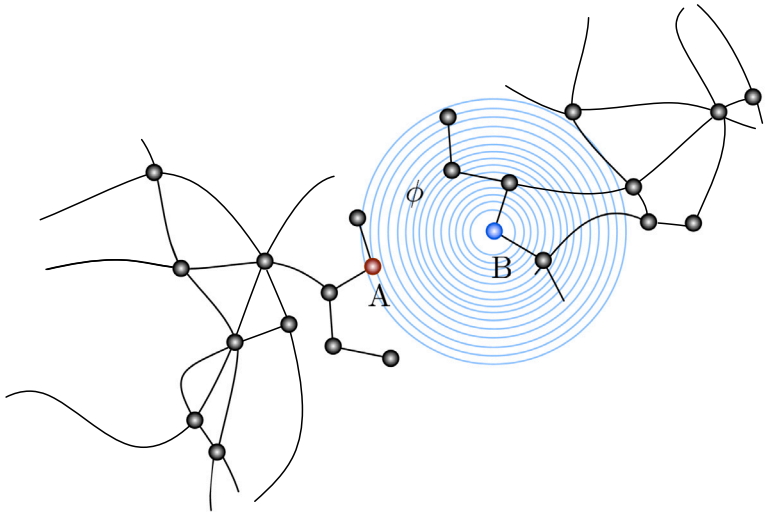


Fig. 3. Interaction between different material particles in a polymer network.

4.1. Nonlocal free energy

In our work, nonlocal continuum mechanics provides a remedy for the loss of ellipticity after the onset of phase transition. To this end, consider a material particle A in the polymer network (Fig. 3). Even though material particle A is at a certain distance from another material particle B, it is located within the interaction potential ϕ_i of B.

Such interaction field can be considered as an electric field whose internal energy density (see e.g. [51]) can be derived as

$$U_{\phi_i} = \frac{1}{2}\beta \left\| -\mathrm{Grad}\phi_i \right\|^2 = \frac{1}{2}\beta \mathrm{Grad}\phi_i \cdot \mathrm{Grad}\phi_i, \quad i = 1, 2 \tag{30}$$

where β is the interaction permittivity representing the ability of the interaction field to spread throughout the polymer. For the sake of simplicity, we normalize the nonlocal interaction potential ϕ_i so that it is dimensionless. Accordingly, β has the force unit [N].

Thus, the total internal energy of natural rubbers can be written as

$$\widehat{U}\left(\phi_1, \phi_2, T, \boldsymbol{\Xi}\right) = U_{\mathbf{F}}\left(\phi_1, \phi_2, \boldsymbol{\Xi}\right) + c_0\left(T - T_0\right) + \sum_{i=1}^{2} \frac{\beta}{2}\mathrm{Grad}\phi_i \cdot \mathrm{Grad}\phi_i + \sum_{i=1}^{2} \frac{E}{2}\phi_i^2. \tag{31}$$

The third term in (31) serves as the internal energy due to nonlocal interactions between molecular particles. In the dimensionless formulation of ϕ_i, the forth term represents the internal energy arising from molecular bond deformations [52] after the onset of SIC, where E [MPa] denotes the Young modulus of molecular bond. From the electric point of view, this term corresponds to the stored energy in the natural rubber capacitor. The nonlocal free energy for natural rubbers can now be given by

$$\begin{aligned} \widehat{\Psi}\left(\mathbf{F}, \phi_1, \phi_2, T, \boldsymbol{\Xi}\right) &= \widehat{U}\left(\phi_1, \phi_2, T, \boldsymbol{\Xi}\right) - T\widetilde{\eta}\left(\mathbf{F}, \phi_1, \phi_2, T, \boldsymbol{\Xi}\right) \\ &= \widetilde{\Psi}\left(\mathbf{F}, \phi_1, \phi_2, T, \boldsymbol{\Xi}\right) + \sum_{i=1}^{2}\left(\frac{\beta}{2}\mathrm{Grad}\phi_i \cdot \mathrm{Grad}\phi_i + \frac{E}{2}\phi_i^2\right). \end{aligned} \tag{32}$$

In this context, $\widetilde{\eta} = \widetilde{\eta}\left(\mathbf{F}, \phi_1, \phi_2, T, \boldsymbol{\Xi}\right)$ and $\widetilde{\Psi} = \widetilde{\Psi}\left(\mathbf{F}, \phi_1, \phi_2, T, \boldsymbol{\Xi}\right)$ adopt the same form as the local entropy of a natural rubber network (13) and the local free energy (20), with the nonlocal variable ϕ_i replacing the principal strains ε_i, $i = 1, 2$, respectively. Moreover, since the nonlocal scalar variables ϕ_i are independent of the change of observer frame, the free energy (32) automatically satisfies the principle of material frame indifference. Furthermore, the internal variables are defined according to the theory of analytical inelasticity [16,38,41,42,53] as

$$\Lambda_i^{\mathrm{c\,max}} = \max_{\tau \in \left[t_i^{\mathrm{c}}, t\right]} \phi_i(\tau) + 1, \quad i = 1, 2. \tag{33}$$

4.2. Laws of thermodynamics

The global form of the first law of thermodynamics can be written in the Lagrangian description as follows (cf. [38])

$$\frac{d}{dt}\int_{\mathcal{B}_0} \widehat{U}\, dV = \int_{\mathcal{B}_0} \mathbf{P} : \dot{\mathbf{F}} dV + \sum_{i=1}^{2}\left(\int_{\mathcal{B}_0} E\varepsilon_i \dot{\phi}_i dV + \int_{\partial\mathcal{B}_0} \beta \mathrm{Grad}\phi_i \cdot \boldsymbol{N}\dot{\phi}_i dA\right) - \int_{\partial\mathcal{B}_0} \boldsymbol{Q}\cdot\boldsymbol{N} dA + \int_{\mathcal{B}_0} \widehat{R} dV, \tag{34}$$

where $E\varepsilon_i$ [MPa] can be interpreted as the short-range volumetric force field, and the term $-\beta \mathrm{Grad}\phi_i \cdot \boldsymbol{N}$ can be translated to the magnitude of the long-range electric field vector. $\boldsymbol{Q}$ is the heat influx per unit reference area, and $\widehat{R}$ denotes the heat supply per unit reference volume of the body. The heat supply for natural rubbers is given by $\widehat{R} = \Delta h \dot{\zeta}$ [16], where Δh is the enthalpy of fusion coefficient.

Using the divergence theorem, the local form of the first law can be formulated as

$$\dot{\hat{U}} = \mathbf{P} : \dot{\mathbf{F}} + \sum_{i=1}^{2} \left(E\varepsilon_i \dot{\phi}_i + \mathrm{Div}\left(\dot{\phi}_i \beta \mathrm{Grad}\phi_i \right) \right) - \mathrm{Div}\boldsymbol{Q} + \widehat{R}. \tag{35}$$

On the other hand, the local form of the second law of thermodynamics for natural rubbers can be given by

$$T\dot{\eta} + \mathrm{Div}\boldsymbol{Q} - \widehat{R} - \frac{1}{T}\boldsymbol{Q} \cdot \mathrm{Grad}T \geq 0. \tag{36}$$

In view of (35), the second law can be written as follows

$$T\dot{\eta} + \mathbf{P} : \dot{\mathbf{F}} + \sum_{i=1}^{2} \left(E\varepsilon_i \dot{\phi}_i + \mathrm{Div}\left(\dot{\phi}_i \beta \mathrm{Grad}\phi_i \right) \right) - \dot{\hat{U}} - \frac{1}{T}\boldsymbol{Q} \cdot \mathrm{Grad}T \geq 0. \tag{37}$$

Since heat transfers from a region of high temperature to another region of lower temperature, $-\boldsymbol{Q} \cdot \mathrm{Grad}T \geq 0$. Thus, a sufficient condition for the second law can be written as

$$\mathcal{D}^{\mathrm{int}} = T\dot{\eta} + \mathbf{P} : \dot{\mathbf{F}} + \sum_{i=1}^{2} \left(E\varepsilon_i \dot{\phi}_i + \mathrm{Div}\left(\dot{\phi}_i \beta \mathrm{Grad}\phi_i \right) \right) - \dot{\hat{U}} \geq 0. \tag{38}$$

Remark 3. Note that, unlike the second law of thermodynamics, the sufficient condition of the Clausius-Duhem inequality [54] is not a first principle of physics, but rather a strong mathematical condition. Consequently, the internal dissipation defined for mathematical convenience in such condition does not always correspond to the irreversibility observed in stress–strain curves of materials [16]. Therefore, it is unsurprising that when this internal dissipation is zero, irreversibility may still occur in the material response, as is evident in strain-induced crystallizing polymers like unfilled natural rubbers [15].

Keeping in mind the identity $\mathrm{Div}(\alpha \boldsymbol{B}) = \boldsymbol{B} \cdot \mathrm{Grad}\alpha + \alpha \mathrm{Div}\boldsymbol{B}$, the internal dissipation $\mathcal{D}^{\mathrm{int}}$ can be further expressed as

$$\mathcal{D}^{\mathrm{int}} = \mathbf{P} : \dot{\mathbf{F}} + \sum_{i=1}^{2} \left(E\varepsilon_i - E\phi_i + \mathrm{Div}\left(\beta \mathrm{Grad}\phi_i \right) - \frac{\partial \widetilde{\Psi}}{\partial \phi_i} \right) \dot{\phi}_i - \frac{\partial \widetilde{\Psi}}{\partial \mathbf{F}} : \dot{\mathbf{F}} - \frac{\partial \hat{U}}{\partial T}\dot{T} + T\frac{\partial \eta}{\partial T}\dot{T} - \frac{\partial \tilde{\Psi}}{\partial \boldsymbol{\Xi}} : \dot{\boldsymbol{\Xi}} \geq 0. \tag{39}$$

Since the internal dissipation of unfilled natural rubbers is always zero [15,16] and take into account the incompressibility constraint, the sufficiency for (39) can be given by

$$\begin{aligned}
&\mathbf{P} = \frac{\partial \widetilde{\Psi}}{\partial \mathbf{F}} - p\mathbf{F}^{-\mathrm{T}}, \\
&E\varepsilon_1 = E\phi_1 - \mathrm{Div}\left(\beta \mathrm{Grad}\phi_1 \right) + \frac{\partial \widetilde{\Psi}}{\partial \phi_1} \\
&E\varepsilon_2 = E\phi_2 - \mathrm{Div}\left(\beta \mathrm{Grad}\phi_2 \right) + \frac{\partial \widetilde{\Psi}}{\partial \phi_2} \\
&\frac{\partial \hat{U}}{\partial T} = T\frac{\partial \eta}{\partial T}, \\
&\mathcal{D}^{\mathrm{int}} = -\frac{\partial \tilde{\Psi}}{\partial \boldsymbol{\Xi}} : \dot{\boldsymbol{\Xi}} = 0.
\end{aligned} \tag{40}$$

The last two conditions in (40) are automatically fulfilled by the fundamental thermodynamic definition of the Helmholtz free energy (see also (12) and (19)) and the property (10).

Remark 4. To the best of our knowledge, our theory represents the first thermodynamically consistent regularization method for natural rubbers that perfectly aligns with calorimetric experimental evidence. Moreover, our formulation inherently satisfies the second law of thermodynamics without imposing any additional constraints on the nonlocal variable. Finally, all parameters within the theory, including nonlocal parameters, are measurable and possess clear physical meaning.

Finally, in view of (40), the first law (35), the internal energy (31) and the Fourier law of heat transfer, the strong form of the equilibrium equations for displacement, temperature and interaction fields can therefore be written as

$$\begin{aligned}
&\mathrm{Div}\mathbf{P} + \boldsymbol{B} = \mathbf{0} && \text{in} \quad \mathcal{B}_0, \\
&\mathbf{P}\boldsymbol{N} = \overline{\boldsymbol{T}} && \text{on} \quad \partial\mathcal{B}_0^T, \\
&\boldsymbol{u} = \overline{\boldsymbol{u}} && \text{on} \quad \partial\mathcal{B}_0^u,
\end{aligned} \tag{41}$$

$$c_0\dot{T} - \mathrm{Div}\left(\mathbf{K}_0 \mathrm{Grad}T \right) = \mathbf{P} : \dot{\mathbf{F}} - \dot{U}_{\mathbf{F}} + \Delta h \dot{\zeta} + \sum_{i=1}^{2} \frac{\partial \widetilde{\Psi}}{\partial \phi_i}\dot{\phi}_i \quad \text{in} \quad \mathcal{B}_0, \tag{42}$$

$$
\begin{aligned}
&T = \overline{T} && \text{on} \quad \partial\mathcal{B}_0^{\theta},\\
&-\mathbf{K}_0 \mathrm{Grad} T \cdot \boldsymbol{N} = \overline{Q} && \text{on} \quad \partial\mathcal{B}_0^{\boldsymbol{Q}},\\
&E\phi_1 - \mathrm{Div}\left(\beta \mathrm{Grad}\phi_1\right) + \frac{\partial \widetilde{\Psi}}{\partial \phi_1} = E\varepsilon_1 && \text{in} \quad \mathcal{B}_0, \qquad (43)\\
&-\beta \mathrm{Grad}\phi_1 \cdot \boldsymbol{N} = 0 && \text{on} \quad \partial\mathcal{B}_0,\\
&E\phi_2 - \mathrm{Div}\left(\beta \mathrm{Grad}\phi_2\right) + \frac{\partial \widetilde{\Psi}}{\partial \phi_2} = E\varepsilon_2 && \text{in} \quad \mathcal{B}_0, \qquad (44)\\
&-\beta \mathrm{Grad}\phi_2 \cdot \boldsymbol{N} = 0 && \text{on} \quad \partial\mathcal{B}_0,
\end{aligned}
$$

where $\boldsymbol{B}$ is the referential body force vector, $\overline{T}$ is the applied traction on the boundary $\partial\mathcal{B}_0^T$, and $\overline{\boldsymbol{u}}$ is the prescribed displacement vector on the boundary $\partial\mathcal{B}_0^u$. In (42), the Lagrangian heat conduction tensor is given by $\mathbf{K}_0(\mathbf{C}) = \det\mathbf{F}\,\mathbf{F}^{-1}k\mathbf{I}\mathbf{F}^{-\mathrm{T}} = k\mathbf{C}^{-1}\det\mathbf{F}$ due to the isotropic assumption of thermal conductivity. The homogeneous Neumann boundary condition is applied for the nonlocal variable ϕ_i as according to Section 4.1, the interaction field can only be effective within the material. Furthermore, in view of (21), the first Piola–Kirchhoff stress tensor can be written as

$$
\mathbf{P}\left(\mathbf{F},\,\phi_1,\,\phi_2,\,T,\,\Xi\right) = -N_{\mathrm{c}}\left(\phi_1,\,\phi_2,\,\Xi\right)T\frac{\partial s_{\mathbf{F}}\left(\mathbf{F},\,\phi_1,\,\phi_2\right)}{\partial \mathbf{F}} - p\mathbf{F}^{-\mathrm{T}}. \qquad (45)
$$

Remark 5. The balance equation for nonlocal variables (43) and (44) can alternatively be expressed as $\phi_i - \mathrm{Div}\left(\frac{\beta}{E}\mathrm{Grad}\phi_i\right) + \frac{1}{E}\frac{\partial\widetilde{\Psi}}{\partial\phi_i} = \varepsilon_i$, with i = 1,2, where the parameter $\frac{\beta}{E}$ has the unit of length squared. This is similar to the dimensionless formulations commonly found in nonlocal continuum theories [25,26,55]. However, we favor the current forms of (43) and (44), because they facilitate the measurement of nonlocal parameters: E as the Young modulus of molecular bond and β as the interaction permittivity.

Remark 6. The calculation of the material time derivative of the internal energy due to deformation is required in the first law of thermodynamics (42). In view of (21) and the definition of the internal variable, $\dot{U}_{\mathbf{F}}$ can be determined under unloading as

$$
\dot{U}_{\mathbf{F}} = \sum_{i=1}^{2}\frac{\partial U_{\mathbf{F}}}{\partial\phi_i}\dot{\phi}_i = \sum_{i=1}^{2} T s_{\mathbf{F}}\frac{\partial N_{\mathrm{c}}}{\partial\phi_i}\dot{\phi}_i. \qquad (46)
$$

For ease of reference, Table 2 summarizes the unknown fields, primary variables, internal variables, thermodynamic variables, and auxiliary variables employed in the formulation.

5. Alternative formulation for the nearly incompressible case

The full incompressibility constraint may lead to poor convergence in standard finite element implementations. Therefore, it can be relaxed to obtain a computationally more efficient and robust solution through a near incompressibility condition. To characterize the near-incompressibility constraint, we modify the right Cauchy–Green tensor as $\mathbf{C}' = J^{-\frac{2}{3}}\mathbf{C}$ and enforce near incompressibility via a penalty parameter $\mathcal{K}$ in the free energy of volumetric deformation $\widetilde{\Psi}_{\mathrm{vol.}}(J)$. To this end, the free energy for natural rubbers is given by

$$
\widetilde{\Psi}\left(\mathbf{C},\,\phi_1,\phi_2,\,T,\,\Xi\right) = \underbrace{U\left(\phi_1,\phi_2,\,T,\,\Xi\right) - T\widetilde{\eta}\left(\mathbf{C}',\,\phi_1,\,\phi_2,\,T,\,\Xi\right)}_{\widetilde{\Psi}_{\mathrm{iso.}}(\mathbf{C}',\phi_1,\phi_2,T,\Xi)} + \widetilde{\Psi}_{\mathrm{vol.}}(J). \qquad (47)
$$

Therein, the volumetric part is expressed as

$$
\widetilde{\Psi}_{\mathrm{vol.}}(J) = \frac{\mathcal{K}}{4}\left(J^2 - 1 - 2\ln J\right). \qquad (48)
$$

The internal energy in (47) can be expressed as

$$
U\left(\phi_1,\,\phi_2,\,T,\,\Xi\right) = U_{\mathbf{C}}\left(\phi_1,\,\phi_2,\,\Xi\right) + U_{\theta}(T). \qquad (49)
$$

In view of (13), the network entropy can be calculated as

$$
\widetilde{\eta}\left(\mathbf{C}',\,\phi_1,\,\phi_2,\,T,\,\Xi\right) = N_{\mathrm{c}}\left(\phi_1,\,\phi_2,\,\Xi\right)s_{\mathbf{C}}\left(\mathbf{C}',\,\phi_1,\,\phi_2\right) + \eta_{\theta}(T), \qquad (50)
$$

in which the entropy of an individual chain is given by

$$
s_{\mathbf{C}}\left(\mathbf{C}',\,\phi_1,\,\phi_2\right) = -\frac{\mu_{\mathrm{c}0}n}{N_{\mathrm{c}0}T_0}\ln\frac{\frac{\pi}{n}r'\left(\mathbf{C}',\,\phi_1,\,\phi_2\right)}{\sin\left(\frac{\pi}{n}r'\left(\mathbf{C}',\,\phi_1,\,\phi_2\right)\right)} - \frac{\mu_{\mathrm{t}0}}{N_{\mathrm{c}0}T_0}v'\left(\mathbf{C}'\right), \qquad (51)
$$

where r' is a modified measure for the end-to-end distance of semi-crystalline chain

$$
r'\left(\mathbf{C}',\,\phi_1,\,\phi_2\right) = \lambda'\left(\mathbf{C}',\,\phi_1,\,\phi_2\right)\sqrt{n} - \zeta_I\left(\phi_1,\,\phi_2\right)n_{\mathrm{c}}. \qquad (52)
$$

Table 2
Summary of variables used in the computational framework.

Symbol	Description
Unknown fields	
$\boldsymbol{u}$	Displacement field
ϕ_1	Nonlocal interaction potential 1
ϕ_2	Nonlocal interaction potential 2
T	Temperature field
Observable variables	
$\mathbf{F}$	Deformation gradient
$\mathbf{C}$	Right Cauchy–Green tensor
T	Temperature
ϕ_1	Nonlocal interaction potential 1
ϕ_2	Nonlocal interaction potential 2
Internal variables	
$\Lambda_1^{c\,\max}$	Nonlocal internal variable 1
$\Lambda_2^{c\,\max}$	Nonlocal internal variable 2
$\boldsymbol{\Xi} = \left\{\Lambda_1^{c\,\max}, \Lambda_2^{c\,\max}\right\}$	Internal variable abbreviation
Thermodynamic quantities	
$\widetilde{\eta}$	Total entropy of the polymer
$\eta_{\mathbf{F}}$	Deformation-dependent part of the entropy
η_θ	Temperature-dependent part of the entropy
$\widehat{U}$	Total internal energy of the polymer
$U_{\mathbf{F}}$	Deformation-dependent part of the internal energy
U_θ	Temperature-dependent part of the internal energy
U_{ϕ_i}	Nonlocal interaction-dependent part of the internal energy
$\widehat{\Psi}$	Total Helmholtz free energy of the polymer
$\widetilde{\Psi}$	Helmholtz free energy of the polymer after excluding U_{ϕ_i}
ζ	Total crystallinity
ζ_{I}	Primary crystallinity
ζ_{II}	Secondary crystallinity
$\boldsymbol{Q}$	Heat influx vector
$\widehat{R}$	Internal heat supply due to phase transition
Auxiliary quantities	
$\mathbf{P}$	First Piola–Kirchhoff stress tensor
$\mathbf{S}$	Second Piola–Kirchhoff stress tensor
$\mathbb{A}$	First elasticity tensor of 4th order
p	Incompressibility Lagrange multiplier
r	End-to-end distance of the representative polymer molecule
f_r	Force applied on the representative polymer molecule
λ	Microscopic stretch of the polymer molecule
ν	Microscopic tube contraction due to topological constraint
q	Stretch amplification (from strand to molecular level) exponent

The microscopic kinematic measures are defined in a similar manner to (16)

$$\lambda'\left(\mathbf{C}', \phi_1, \phi_2\right) = \left(\sqrt{\frac{I_1'(\mathbf{C}')}{3}}\right)^{q(\phi_1,\phi_2)}, \quad \upsilon'\left(\mathbf{C}'\right) = \sqrt{\frac{I_2'(\mathbf{C}')}{3}}, \tag{53}$$

where the two invariants of the modular tensor $\mathbf{C}'$ are defined by

$$I_1'\left(\mathbf{C}'\right) = \mathbf{C}' : \mathbf{I}, \quad I_2'\left(\mathbf{C}'\right) = \frac{1}{2}\left[\left(\mathbf{C}' : \mathbf{I}\right)^2 - \mathbf{C}' : \mathbf{C}'\right]. \tag{54}$$

The stretch amplification exponent is written as

$$q\left(\phi_1, \phi_2\right) = q_0\left(1 + \zeta_{\mathrm{I}}\left(\phi_1, \phi_2\right)\right). \tag{55}$$

Finally, the strong form of the equilibrium equations for displacement, temperature and interaction fields can also be written in terms of $\mathbf{C}$ as

$$\begin{aligned} &\mathrm{Div}\left(\mathbf{FS}\right) + \boldsymbol{B} = \mathbf{0} && \text{in} \quad \mathcal{B}_0, \\ &\mathbf{FS}\boldsymbol{N} = \overline{\boldsymbol{T}} && \text{on} \quad \partial\mathcal{B}_0^T, \\ &\boldsymbol{u} = \overline{\boldsymbol{u}} && \text{on} \quad \partial\mathcal{B}_0^u, \end{aligned} \tag{56}$$

$$c_0\dot{T} - \mathrm{Div}\left(\mathbf{K}_0 \mathrm{Grad} T\right) = f_T \qquad \text{in} \quad \mathcal{B}_0, \tag{57}$$

$$
\begin{aligned}
&T = \overline{T} && \text{on} \quad \partial\mathcal{B}_0^T,\\
&-\mathbf{K}_0 \mathrm{Grad} T \cdot \boldsymbol{N} = \overline{Q} && \text{on} \quad \partial\mathcal{B}_0^{\boldsymbol{Q}},\\
&E\phi_1 - \mathrm{Div}\left(\beta \mathrm{Grad}\phi_1\right) = f_{\phi_1} && \text{in} \quad \mathcal{B}_0, \qquad (58)\\
&-\beta \mathrm{Grad}\phi_1 \cdot \boldsymbol{N} = 0 && \text{on} \quad \partial\mathcal{B}_0,\\
&E\phi_2 - \mathrm{Div}\left(\beta \mathrm{Grad}\phi_2\right) = f_{\phi_2} && \text{in} \quad \mathcal{B}_0, \qquad (59)\\
&-\beta \mathrm{Grad}\phi_2 \cdot \boldsymbol{N} = 0 && \text{on} \quad \partial\mathcal{B}_0,
\end{aligned}
$$

The second Piola–Kirchhoff stress tensor is decomposed into two parts as follows

$$\mathbf{S} = \mathbf{S}_{\text{vol.}} + \mathbf{S}_{\text{iso.}}, \tag{60}$$

where the explicit expressions of the volumetric and isochoric parts of the second Piola–Kirchhoff stress tensor are given by

$$
\begin{aligned}
&\mathbf{S}_{\text{vol.}} = \frac{\mathcal{K}}{2}\left(J^2 - 1\right)\mathbf{C}^{-1},\\
&\mathbf{S}_{\text{iso.}} = -2N_{\text{c}}T\frac{\partial s_{\mathbf{C}}}{\partial \mathbf{C}}.
\end{aligned} \tag{61}
$$

The driving force for the thermal equation f_T (so-called the heat source) is given by

$$f_T = \mathbf{S} : \frac{1}{2}\dot{\mathbf{C}} - \dot{U}_{\mathbf{C}} + \sum_{i=1}^{2}\frac{\partial \widetilde{\Psi}}{\partial \phi_i}\dot{\phi}_i + \Delta h \dot{\zeta}. \tag{62}$$

Using the definition of the internal variable, the second and the third terms of right hand side of (62) can be written as follow

$$
\begin{aligned}
-\dot{U}_{\mathbf{C}} + \sum_{i=1}^{2}\frac{\partial \widetilde{\Psi}}{\partial \phi_i}\dot{\phi}_i = \quad & \underbrace{\sum_{i=1}^{2}\left[\frac{\partial}{\partial \phi_i}\left(-U_{\mathbf{C}} + \widetilde{\Psi}\right)\right]\dot{\phi}_i}_{-\sum_{i=1}^{2}\left(T N_{\text{c}}\frac{\partial s_{\mathbf{C}}}{\partial \phi_i} + T s_{\mathbf{C}}\frac{\partial N_{\text{c}}}{\partial \phi_i}\right)\dot{\phi}_i} \quad \underbrace{-\sum_{i=1}^{2}\frac{\partial U_{\mathbf{C}}}{\partial \Lambda_i^{\text{c max}}}\dot{\Lambda}_i^{\text{c max}}}_{0},
\end{aligned} \tag{63}
$$

and the time derivative of the total crystallinity reads

$$\dot{\zeta} = \sum_{i=1}^{2}\frac{\partial \zeta}{\partial \phi_i}\dot{\phi}_i. \tag{64}$$

Substituting (63) and (64) in (62), the thermal driving force becomes

$$f_T = \mathbf{S} : \frac{1}{2}\dot{\mathbf{C}} + \sum_{i=1}^{2}\left(-T N_{\text{c}}\frac{\partial s_{\mathbf{C}}}{\partial \phi_i} - T s_{\mathbf{C}}\frac{\partial N_{\text{c}}}{\partial \phi_i} + \Delta h\frac{\partial \zeta}{\partial \phi_i}\right)\dot{\phi}_i. \tag{65}$$

The driving force for the nonlocal equations f_{ϕ_i} are given by

$$f_{\phi_i} = E\varepsilon_i - \frac{\partial \widetilde{\Psi}}{\partial \phi_i}, \quad i = 1, 2, \tag{66}$$

where the maximum and middle principal strains are functions of $\mathbf{C}$ (i.e. $\varepsilon_1 = \varepsilon_1(\mathbf{C})$ and $\varepsilon_2 = \varepsilon_2(\mathbf{C})$).

For latter consideration, the linearization of $\mathbf{S}$ reads as

$$\Delta\mathbf{S} = \mathbb{C}_{uu} : \frac{1}{2}\Delta\mathbf{C} + \mathbf{C}_{uT}\Delta T + \sum_{i=1}^{2}\mathbf{C}_{u\phi_i}\Delta\phi_i, \tag{67}$$

where the fourth order tensor $\mathbb{C}_{uu}$ is defined by

$$\mathbb{C}_{uu} = 2\frac{\partial \mathbf{S}}{\partial \mathbf{C}} = \mathcal{K}J^2\mathbf{C}^{-1}\otimes\mathbf{C}^{-1} + \left(J^2 - 1\right)\frac{\partial \mathbf{C}^{-1}}{\partial \mathbf{C}} - 4N_{\text{c}}T\frac{\partial^2 s_{\mathbf{C}}}{\partial \mathbf{C}\partial \mathbf{C}}. \tag{68}$$

The remaining tangent moduli $\mathbf{C}_{uT}$ and $\mathbf{C}_{u\phi_i}$ are given by

$$\mathbf{C}_{uT} = \frac{\partial \mathbf{S}}{\partial T} = \frac{\mathbf{S}_{\text{iso.}}}{T}, \tag{69}$$

$$\mathbf{C}_{u\phi_i} = \frac{\partial \mathbf{S}}{\partial \phi_i} = -2T N_{\text{c}}\frac{\partial^2 s_{\mathbf{C}}}{\partial \mathbf{C}\partial \phi_i} - 2T\frac{\partial N_{\text{c}}}{\partial \phi_i}\frac{\partial s_{\mathbf{C}}}{\partial \mathbf{C}}, \quad i = 1, 2. \tag{70}$$

Then, the linearization of f_T can be expressed by

$$\Delta f_T = \mathbf{C}_{Tu} : \frac{1}{2}\Delta\mathbf{C} + C_{TT}\Delta T + \sum_{i=1}^{2}C_{T\phi_i}\Delta\phi_i, \tag{71}$$

where the tangent moduli $\mathbf{C}_{Tu}$, C_{TT} and $C_{T\phi_i}$ are given by

$$\mathbf{C}_{Tu} = 2\frac{\partial f_T}{\partial \mathbf{C}} = \mathbb{C}_{uu} : \dot{\mathbf{C}} + \mathbf{S} : \frac{\partial \dot{\mathbf{C}}}{\partial \mathbf{C}} + 2\sum_{i=1}^{2}\left(-TN_{\mathrm{c}}\frac{\partial^2 s_{\mathbf{C}}}{\partial\phi_i\partial\mathbf{C}} - T\frac{\partial N_{\mathrm{c}}}{\partial\phi_i}\frac{\partial s_{\mathbf{C}}}{\partial\mathbf{C}}\right)\dot{\phi}_i, \tag{72}$$

$$C_{TT} = \frac{\partial f_T}{\partial T} = \mathbf{C}_{uT} : \frac{1}{2}\dot{\mathbf{C}} + \sum_{i=1}^{2}\left(-N_{\mathrm{c}}\frac{\partial s_{\mathbf{C}}}{\partial\phi_i} - s_{\mathbf{C}}\frac{\partial N_{\mathrm{c}}}{\partial\phi_i}\right)\dot{\phi}_i, \tag{73}$$

$$\begin{aligned} C_{T\phi_i} = \frac{\partial f_T}{\partial \dot{\phi}_i} = \mathbf{C}_{u\phi_i} : \frac{1}{2}\dot{\mathbf{C}} \\ + \sum_{j=1}^{2}\left(-TN_{\mathrm{c}}\frac{\partial^2 s_{\mathbf{C}}}{\partial\phi_i\partial\phi_j} - T\frac{\partial N_{\mathrm{c}}}{\partial\phi_i}\frac{\partial s_{\mathbf{C}}}{\partial\phi_j} - T\frac{\partial s_{\mathbf{C}}}{\partial\phi_i}\frac{\partial N_{\mathrm{c}}}{\partial\phi_j} - Ts_{\mathbf{C}}\frac{\partial^2 N_{\mathrm{c}}}{\partial\phi_i\partial\phi_j} + \Delta h\frac{\partial^2\zeta}{\partial\phi_i\partial\phi_j}\right)\dot{\phi}_j \\ + \left(-TN_{\mathrm{c}}\frac{\partial s_{\mathbf{C}}}{\partial\phi_i} - Ts_{\mathbf{C}}\frac{\partial N_{\mathrm{c}}}{\partial\phi_i} + \Delta h\frac{\partial\zeta}{\partial\phi_i}\right)\frac{\partial\dot{\phi}_i}{\partial\phi_i}. \end{aligned} \tag{74}$$

Finally, the linearization of the driven force for the nonlocal fields can be expressed by

$$\Delta f_{\phi_i} = \mathbf{C}_{\phi_i u} : \frac{1}{2}\Delta\mathbf{C} + C_{\phi_i T}\Delta T + \sum_{j=1}^{2} C_{\phi_i\phi_j}\Delta\phi_j, \tag{75}$$

where the tangent moduli $\mathbf{C}_{\phi_i u}$, $C_{\phi_i T}$ and $C_{\phi_i\phi_j}$ are given by

$$\mathbf{C}_{\phi_i u} = 2\frac{\partial f_{\phi_i}}{\partial\mathbf{C}} = 2E\frac{\partial\varepsilon_i}{\partial\mathbf{C}} - 2\frac{\partial^2\widetilde{\Psi}}{\partial\mathbf{C}\partial\phi_i}, \quad i = 1,2, \tag{76}$$

$$C_{\phi_i T} = -\frac{\partial^2\widetilde{\Psi}}{\partial T\partial\phi_i}, \quad i = 1,2, \tag{77}$$

$$C_{\phi_i\phi_j} = -\frac{\partial^2\widetilde{\Psi}}{\partial\phi_i\partial\phi_j}, \quad i,j = 1,2. \tag{78}$$

6. Mixed finite element formulation

The weak forms of the governing Eqs. (56)–(59) can be constructed from the elemental contributions to the different fields

$$\begin{aligned} \delta\Pi = \sum_{e=1}^{N_{el}}\left(\delta\Pi_e^{\text{mechanical,int.}} + \delta\Pi_e^{\text{thermal,int.}} + \delta\Pi_e^{\text{nonlocal}}\right) \\ - \sum_{e=1}^{N_{el}}\left(\delta\Pi_e^{\text{mechanical,ext.}} + \delta\Pi_e^{\text{thermal,ext.}}\right) = 0, \end{aligned} \tag{79}$$

where N_{el} is the number of elements in the mesh. The term $\delta\Pi_e^{\text{mechanical,ext.}}$ represents the virtual work done by the external forces, and $\delta\Pi_e^{\text{thermal,ext.}}$ represents the contribution of the external heat flux to the boundary. The variation of the mechanical part $\delta\Pi_e^{\text{mechanical,int.}}$ represents the contribution of the free energy and can be derived by using the Hu–Washizu variational principle. It is well known that the standard Bubnov–Galerkin approach exhibits severe volumetric locking when modeling nearly incompressible materials. For eliminating this pathology, the point-wise dilatation measure is replaced by an average one, while the distortional part remains valid point-wise. Specifically, the assumed deformation measure is formulated as follows

$$\overline{\mathbf{C}} = \left(\frac{\overline{J}}{J}\right)^{2/3}\mathbf{C}, \quad \det\overline{\mathbf{C}} = \overline{J}^2. \tag{80}$$

The Hu–Washizu variational principle of the mechanical field is given by

$$\delta\Pi_e^{\text{mechanical,int.}} = \int_{\Omega_e^0}\overline{\mathbf{S}} : \frac{1}{2}\delta\overline{\mathbf{C}}\, d\Omega_e^0 + \delta\int_{\Omega_e^0}\overline{p}\left(J - \overline{J}\right) d\Omega_e^0, \tag{81}$$

where the fields $\overline{J}$ and $\overline{p}$ are, respectively, related to the volume change and the hydrostatic pressure. $\overline{\mathbf{S}}$ is the total second Piola–Kirchhoff stress tensor evaluated using the modified right Cauchy–Green deformation tensor $\overline{\mathbf{C}}$ and the assumed volumetric dilatation $\overline{J}$. Supposing that the assumed fields $\overline{J}$ and $\overline{p}$ are constants at the element level, enforcing stationarity of (81) at the element level yields the following explicit expression for the assumed volume change field

$$\overline{J} = \frac{1}{\Omega_e^0}\int_{\Omega_e^0} J\, d\Omega_e^0. \tag{82}$$

Eq. (82) implies $\overline{J}$ represents the average volume change. Adopting the expressions (82), the reduced form of the variation of the mechanical part can be re-written as

$$\delta\Pi_{\text{reduced},e}^{\text{mechanical,int.}} = \int_{\Omega_e^0}\overline{\mathbf{S}} : \frac{1}{2}\delta\overline{\mathbf{C}}\, d\Omega_e^0, \tag{83}$$

where the variation of the modified right Cauchy–Green tensor $\delta\bar{\mathbf{C}}$ reads

$$\delta\overline{\mathbf{C}} = \left(\frac{\overline{J}}{J}\right)^{2/3}\delta\mathbf{C} + \frac{2}{3}\left(\frac{\delta\overline{J}}{\overline{J}} - \frac{\delta J}{J}\right)\overline{\mathbf{C}}. \tag{84}$$

However, one has to keep in mind that $\overline{J}$ in (83) is no longer an independent field. Using the relationship $J^2 = \det\mathbf{C}$ and the explicit form for the average of the volume change field yields the following expression for the variation of J and $\overline{J}$

$$\begin{aligned}\delta J &= \frac{1}{2}J\mathbf{C}^{-1} : \delta\mathbf{C},\\ \delta\overline{J} &= \frac{1}{\Omega_e^0}\int_{\Omega_e^0}\delta J\, d\Omega_e^0.\end{aligned} \tag{85}$$

The variations of the thermal part $\delta\Pi_e^{\text{thermal}}$ and the nonlocal $\delta\Pi_e^{\text{nonlocal}}$ parts can be obtained from the strong form by multiplying the governing equations with the variations of the corresponding fields, δT, $\delta\phi_1$, and $\delta\phi_2$, followed by the application of Gauss theorem. Specifically, the variation of the thermal part $\delta\Pi_e^{\text{thermal}}$ is given by

$$\delta\Pi_e^{\text{thermal}} = \int_{\Omega_e^0}\left[c_0\dot{T}\delta T + \left(\mathbf{K}_0\text{Grad}T\right)\cdot\text{Grad}\delta T - \overline{f}_T\delta T\right]\, d\Omega_e^0, \tag{86}$$

where the driving force for the thermal field $\overline{f}_T$ is evaluated using $\overline{\mathbf{C}}$ and $\overline{J}$. The variation of the nonlocal fields $\delta\Pi_e^{\text{nonlocal}}$ is given by

$$\delta\Pi_e^{\text{nonlocal}} = \sum_{i=1}^{2}\int_{\Omega_e^0}\left[E\phi_i\delta\phi_i + \beta\text{Grad}\phi_i\cdot\text{Grad}\delta\phi_i - \overline{f}_{\phi_i}\delta\phi_i\right]\, d\Omega_e^0, \tag{87}$$

where the driving forces for the nonlocal equation $\overline{f}_{\phi_i}$ corresponding to the field ϕ_i are also evaluated in terms of $\overline{\mathbf{C}}$ and $\overline{J}$.

Next, in order to derive the stiffness matrices, a linearization of the variation given in (79) is introduced

$$\Delta\delta\Pi = \sum_{e=1}^{N_{el}}\left(\Delta\delta\Pi_{\text{reduced},e}^{\text{mechanical,int}} + \Delta\delta\Pi_e^{\text{thermal}} + \Delta\delta\Pi_e^{\text{nonlocal}}\right). \tag{88}$$

The linearization of the mechanical part $\Delta\delta\Pi_{\text{reduced},e}^{\text{mechanical,int}}$ has the form as

$$\Delta\delta\Pi_{\text{reduced},e}^{\text{mechanical,int}} = \int_{\Omega_e^0}\left(\frac{1}{2}\delta\overline{\mathbf{C}} : \overline{\mathbb{C}} : \frac{1}{2}\Delta\overline{\mathbf{C}} + \overline{\mathbf{S}} : \frac{1}{2}\Delta\delta\overline{\mathbf{C}}\right)\, d\Omega_e^0 + \int_{\Omega_e^0}\frac{1}{2}\delta\overline{\mathbf{C}} : \overline{\mathbf{C}}_{uT}\Delta T\, d\Omega_e^0 + \sum_{j=1}^{2}\int_{\Omega_e^0}\frac{1}{2}\delta\overline{\mathbf{C}} : \overline{\mathbf{C}}_{u\phi_j}\Delta\phi_j\, d\Omega_e^0. \tag{89}$$

In (89), the linearization of the variations of the modified right Cauchy–Green deformation tensor can be expressed by

$$\begin{aligned}\Delta\delta\overline{\mathbf{C}} = &\left(\frac{\overline{J}}{J}\right)^{2/3}\Delta\delta\mathbf{C} + \frac{2}{3}\left[\frac{\delta\overline{J}}{\overline{J}} - \frac{\delta J}{J}\right]\Delta\overline{\mathbf{C}} + \frac{2}{3}\left[\frac{\Delta\overline{J}}{\overline{J}} - \frac{\Delta J}{J}\right]\delta\overline{\mathbf{C}}\\ &+ \frac{2}{3}\left[\frac{\Delta\delta\overline{J}}{\overline{J}} - \frac{\Delta\delta J}{J} - \frac{5}{3}\frac{\delta\overline{J}}{\overline{J}}\frac{\Delta\overline{J}}{\overline{J}} + \frac{1}{3}\frac{\delta J}{J}\frac{\Delta J}{J} + \frac{2}{3}\frac{\delta\overline{J}}{\overline{J}}\frac{\Delta J}{J} + \frac{2}{3}\frac{\delta J}{J}\frac{\Delta\overline{J}}{\overline{J}}\right]\overline{\mathbf{C}},\end{aligned} \tag{90}$$

where the linearization of the variation of the volume change and its average are defined by

$$\begin{aligned}\Delta\delta J &= J\mathbf{C}^{-1} : \frac{1}{2}\Delta\delta\mathbf{C} + \frac{1}{2}\delta\mathbf{C} : \left(J\mathbf{C}^{-1}\otimes\mathbf{C}^{-1}\right) : \frac{1}{2}\Delta\mathbf{C} + J\Delta\mathbf{C}^{-1} : \frac{1}{2}\delta\mathbf{C},\\ \Delta\delta\overline{J} &= \frac{1}{\Omega_e^0}\int_{\Omega_e^0}\Delta\delta J\, d\Omega_e^0.\end{aligned} \tag{91}$$

Moreover, the linearization of the variation of the thermal contribution $\delta\Pi_e^{\text{thermal}}$ can be written as

$$\begin{aligned}\Delta\delta\Pi_e^{\text{thermal}} = &\int_{\Omega_e^0}\left(\left(\text{Grad}\delta T\otimes\text{Grad}T\right) : \overline{\mathbb{C}}_{\mathbb{K}_0} : \frac{1}{2}\Delta\overline{\mathbf{C}} - \delta T\overline{\mathbf{C}}_{Tu} : \frac{1}{2}\Delta\overline{\mathbf{C}}\right)\, d\Omega_e^0\\ &+ \int_{\Omega_e^0}\left(\delta T c_0\Delta\dot{T} + \text{Grad}\delta T\cdot\mathbf{K}_0\cdot\text{Grad}\Delta T - \delta T\overline{C}_{TT}\Delta T\right)\, d\Omega_e^0\\ &- \sum_{j=1}^{2}\int_{\Omega_e^0}\delta T\overline{C}_{T\phi_j}\Delta\phi_j\, d\Omega_e^0,\end{aligned} \tag{92}$$

where the fourth-order tensor $\overline{\mathbb{C}}_{\mathbb{K}_0}$ represents the linearization of the heat conductivity tensor $\overline{\mathbf{K}}_0 = k\overline{J}\,\overline{\mathbf{C}}^{-1}$ with respect to $\overline{\mathbf{C}}$

$$\overline{\mathbb{C}}_{\mathbb{K}_0} = 2\frac{\partial\overline{\mathbf{K}}_0}{\partial\overline{\mathbf{C}}} = 2\overline{J}k\frac{\partial\overline{\mathbf{C}}^{-1}}{\partial\overline{\mathbf{C}}} + \overline{J}k\overline{\mathbf{C}}^{-1}\otimes\overline{\mathbf{C}}^{-1}. \tag{93}$$

In terms of the nonlocal fields, the linearization of the variation of the potential energy $\delta \Pi_e^{\text{nonlocal}}$ takes the following form

$$\begin{aligned}\Delta\delta \Pi_e^{\text{nonlocal}} = &- \sum_{i=1}^{2} \int_{\Omega_e^0} \delta\phi_i \overline{\mathbf{C}}_{\phi_i u} : \frac{1}{2} \Delta\overline{\mathbf{C}}\, d\Omega_e^0 - \sum_{i=1}^{2} \int_{\Omega_e^0} \delta\phi_i \overline{C}_{\phi_i T} \Delta T\, d\Omega_e^0 \\ &+ \sum_{i=1}^{2}\sum_{j=1}^{2} \int_{\Omega_e^0} \left(\delta\phi_i E \delta_{ij} \Delta\phi_j + \beta\delta_{ij} \text{Grad}\delta\phi_i \cdot \text{Grad}\Delta\phi_j - \delta\phi_i \overline{C}_{\phi_i\phi_j} \Delta\phi_j \right) d\Omega_e^0,\end{aligned} \tag{94}$$

For the finite element derivations, we apply in the following the Voigt notation. Vectors and second-order tensors are stored as arrays, indicated by a single underline. Fourth-order tensors are transformed into matrices specified by a double underline. In this study, the trilinear shape functions of a 3D 8-node cube element are chosen to approximate displacement field, thermal field and the nonlocal fields as well as their variations. Accordingly,

$$\underline{\boldsymbol{u}} = \sum_{I=1}^{N_{en}} N_I \underline{\widehat{\boldsymbol{u}}}_e^I, \quad \delta\underline{\boldsymbol{u}} = \sum_{I=1}^{N_{en}} N_I \delta\underline{\widehat{\boldsymbol{u}}}_e^I \tag{95}$$

$$T = \sum_{I=1}^{N_{en}} N_I \widehat{T}_e^I, \quad \delta T = \sum_{I=1}^{N_{en}} N_I \delta\widehat{T}_e^I, \tag{96}$$

$$\phi_i = \sum_{I=1}^{N_{en}} N_I \widehat{\phi}_{ie}^I, \quad \delta\phi_i = \sum_{I=1}^{N_{en}} N_I \delta\widehat{\phi}_{ie}^I, \tag{97}$$

where N_I are the trilinear shape functions, and $N_{en} = 8$ is the number of nodes of the finite element. Furthermore, $\{\underline{\widehat{\boldsymbol{u}}}_e^I, \widehat{T}_e^I, \widehat{\phi}_{1e}^I, \widehat{\phi}_{2e}^I\}$ are the displacement vector, the temperature field, and the nonlocal fields at node I, respectively, while $\{\delta\underline{\widehat{\boldsymbol{u}}}_e^I, \delta\widehat{T}_e^I, \delta\widehat{\phi}_{1e}^I, \delta\widehat{\phi}_{2e}^I\}$ denote their corresponding variations. Then, the variation of the Green–Lagrange strain $\delta\underline{\mathbf{E}} = \frac{1}{2}\delta\underline{\mathbf{C}} = \left\{\delta E_{11}, \delta E_{22}, \delta E_{33}, 2\delta E_{12}, 2\delta E_{13}, 2\delta E_{23}\right\}^{\mathrm{T}}$, together with the gradients of the temperature $\text{Grad}\delta T = \{\frac{\partial\delta T}{\partial X_1}, \frac{\partial\delta T}{\partial X_2}, \frac{\partial\delta T}{\partial X_3}\}^{\mathrm{T}}$ and of the variation of the nonlocal fields $\text{Grad}\phi_i = \{\frac{\partial\delta\phi_i}{\partial X_1}, \frac{\partial\delta\phi_i}{\partial X_2}, \frac{\partial\delta\phi_i}{\partial X_3}\}^{\mathrm{T}}, (i = 1, 2)$, are given by

$$\delta\underline{\mathbf{E}} = \sum_{I=1}^{N_{en}} \underline{\underline{\mathbf{B}}}_{uI} \underline{\widehat{\boldsymbol{u}}}_e^I = \underline{\underline{\mathbf{B}}}_u \delta\underline{\widehat{\boldsymbol{U}}}_e, \tag{98}$$

$$\text{Grad}\delta T = \sum_{I=1}^{N_{en}} \underline{\mathbf{B}}_{TI} \delta\widehat{T}_e^I = \underline{\underline{\mathbf{B}}}_T \delta\underline{\widehat{\boldsymbol{T}}}_e, \tag{99}$$

$$\text{Grad}\delta\phi_i = \sum_{I=1}^{N_{en}} \underline{\mathbf{B}}_{\phi I} \delta\widehat{\phi}_{ie}^I = \underline{\underline{\mathbf{B}}}_{\phi} \delta\underline{\widehat{\boldsymbol{\phi}}}_{ie}, \tag{100}$$

The matrices $\underline{\underline{\mathbf{B}}}_u = \left[\underline{\underline{\mathbf{B}}}_{u1}, \ldots, \underline{\underline{\mathbf{B}}}_{uN_{en}}\right]$, $\underline{\underline{\mathbf{B}}}_T = \left[\underline{\mathbf{B}}_{T1}, \ldots, \underline{\mathbf{B}}_{TN_{en}}\right]$ and $\underline{\underline{\mathbf{B}}}_{\phi} = \left[\underline{\mathbf{B}}_{\phi 1}, \ldots, \underline{\mathbf{B}}_{\phi N_{en}}\right]$ consist, respectively, of the matrices $\underline{\underline{\mathbf{B}}}_{uI}$, $\underline{\mathbf{B}}_{TI}$ and $\underline{\mathbf{B}}_{\phi I}$, which are given by

$$\underline{\underline{\mathbf{B}}}_{uI} = \begin{bmatrix} F_{11}N_{I,1} & F_{21}N_{I,1} & F_{31}N_{I,1} \\ F_{12}N_{I,2} & F_{22}N_{I,2} & F_{32}N_{I,2} \\ F_{13}N_{I,3} & F_{23}N_{I,3} & F_{33}N_{I,3} \\ F_{11}N_{I,2} + F_{12}N_{I,1} & F_{21}N_{I,2} + F_{22}N_{I,1} & F_{31}N_{I,2} + F_{32}N_{I,1} \\ F_{12}N_{I,3} + F_{13}N_{I,2} & F_{22}N_{I,3} + F_{23}N_{I,2} & F_{32}N_{I,3} + F_{33}N_{I,2} \\ F_{11}N_{I,3} + F_{13}N_{I,1} & F_{21}N_{I,3} + F_{23}N_{I,1} & F_{31}N_{I,3} + F_{33}N_{I,1} \end{bmatrix}, \quad \underline{\mathbf{B}}_{TI} = \underline{\mathbf{B}}_{\phi I} = \begin{Bmatrix} N_{I,1} \\ N_{I,2} \\ N_{I,3} \end{Bmatrix}, \tag{101}$$

where F_{ij} are components of deformation gradient $\mathbf{F}$ and $N_{I,i} = \frac{\partial N_I}{\partial X_i}$ are the derivatives of shape functions with respect to referential coordinates. Substituting (98) into $(85)_1$ and $(85)_2$, we express the variation of point-wise dilatation and its volume average in terms of the virtual nodal displacements such as

$$\begin{aligned}\delta J &= \delta\underline{\widehat{\boldsymbol{U}}}_e^{\mathrm{T}} \underline{\mathbf{a}}_1, \quad \underline{\mathbf{a}}_1 = J\underline{\underline{\mathbf{B}}}_u^{\mathrm{T}} \underline{\mathbf{C}}^{-1}, \\ \delta\overline{J} &= \delta\underline{\widehat{\boldsymbol{U}}}_e^{\mathrm{T}} \overline{\underline{\mathbf{a}}}_1, \quad \overline{\underline{\mathbf{a}}}_1 = \frac{1}{\Omega_e^0} \int_{\Omega_e^0} \underline{\mathbf{a}}_1\, d\Omega_e^0,\end{aligned} \tag{102}$$

in which $\underline{\mathbf{C}}^{-1} = \left\{C^{-1}{}_{11}, C^{-1}{}_{22}, C^{-1}{}_{33}, C^{-1}{}_{12}, C^{-1}{}_{23}, C^{-1}{}_{31}\right\}$ is a column vector consisting of the components of the inverse of the right Cauchy–Green. Using Eqs. (102) and (84), the variation of the modified Green–Lagrange strain $\delta\overline{\underline{\mathbf{E}}}$ can be expressed as

$$\delta\overline{\underline{\mathbf{E}}} = \frac{1}{2}\delta\overline{\underline{\mathbf{C}}} = \overline{\underline{\underline{\mathbf{B}}}}_u \delta\underline{\widehat{\boldsymbol{U}}}_e, \quad \overline{\underline{\underline{\mathbf{B}}}}_u = \left(\frac{\overline{J}}{J}\right)^{2/3} \underline{\underline{\mathbf{B}}}_u + \frac{1}{3}\overline{\underline{\mathbf{C}}}^{\mathrm{T}} \left(\frac{\overline{\underline{\mathbf{a}}}_1}{\overline{J}} - \frac{\underline{\mathbf{a}}_1}{J}\right). \tag{103}$$

Next, the discretized form of the four-field variational formulation can be written as

$$\delta\Pi_e\left(\boldsymbol{u}, T, \phi_1, \phi_2\right) = \delta\underline{\widehat{\boldsymbol{U}}}_e \underline{\widehat{\boldsymbol{f}}}_e^{\,\text{int},u} + \delta\underline{\widehat{\boldsymbol{T}}}_e \underline{\widehat{\boldsymbol{f}}}_e^{\,\text{int},T} + \sum_{i=1}^{2} \delta\underline{\widehat{\boldsymbol{\phi}}}_{ie} \underline{\widehat{\boldsymbol{f}}}_e^{\,\text{int},\phi_i}, \tag{104}$$

where the generalized internal forces $\underline{\hat{f}}_e^{\text{int},u}$, $\underline{\hat{f}}_e^{\text{int},T}$, and $\underline{\hat{f}}_e^{\text{int},\phi_i}$ are given by

$$\begin{aligned}
\underline{\hat{f}}_e^{\text{int},u} &= \int_{\Omega_e^0} \underline{\underline{\overline{\mathbf{B}}}}_u^{\mathrm{T}} \underline{\overline{\mathbf{S}}}\, d\Omega_e^0, \\
\underline{\hat{f}}_e^{\text{int},T} &= \int_{\Omega_e^0} \left[\underline{\boldsymbol{N}}^{\mathrm{T}} \left(c_0 \dot{T} - \overline{f}_T \right) + \underline{\underline{\mathbf{B}}}_I^{\mathrm{T}} \underline{\underline{\overline{\mathbf{K}}}}_0 \operatorname{Grad} T \right] d\Omega_e^0, \\
\underline{\hat{f}}_e^{\text{int},\phi_i} &= \int_{\Omega_e^0} \left[\underline{\boldsymbol{N}}^{\mathrm{T}} \left(E\phi_i - \overline{f}_{\phi_i} \right) + \beta \underline{\underline{\mathbf{B}}}_\phi^{\mathrm{T}} \operatorname{Grad} \phi_i \right] d\Omega_e^0.
\end{aligned} \tag{105}$$

Therein, $\underline{\overline{\mathbf{S}}} = \left\{ \overline{S}_{11}, \overline{S}_{22}, \overline{S}_{33}, \overline{S}_{12}, \overline{S}_{23}, \overline{S}_{31} \right\}^{\mathrm{T}}$ is 6×1 vector consisting of the modified second Piola–Kirchhoff stress components and $\underline{\boldsymbol{N}} = \left\{ N_1, N_2, \ldots, N_{N_{en}} \right\}$ is a vector consisting of the shape functions. Then, in order to develop the tangent stiffness matrix, the discretizations provided in (95), (96), (97), (98), (99), (100), and (103) are substituted into Eqs. (89), (92) and (94). Specifically, the linearization of the variation of the internal potential energy (88), can then be discretized and written as

$$\Delta\delta\Pi_e \left(\mathbf{u}, T, \phi_1, \phi_2 \right) = \left\{ \delta\hat{\underline{U}}_e \quad \delta\hat{\underline{T}}_e \quad \delta\hat{\underline{\phi}}_{1e} \quad \delta\hat{\underline{\phi}}_{2e} \right\}^{\mathrm{T}} \begin{bmatrix} \underline{\underline{\mathbf{K}}}_e^{uu} & \underline{\underline{\mathbf{K}}}_e^{uT} & \underline{\underline{\mathbf{K}}}_e^{u\phi_1} & \underline{\underline{\mathbf{K}}}_e^{u\phi_2} \\ \underline{\underline{\mathbf{K}}}_e^{Tu} & \underline{\underline{\mathbf{K}}}_e^{TT} & \underline{\underline{\mathbf{K}}}_e^{T\phi_1} & \underline{\underline{\mathbf{K}}}_e^{T\phi_2} \\ \underline{\underline{\mathbf{K}}}_e^{\phi_1 u} & \underline{\underline{\mathbf{K}}}_e^{\phi_1 T} & \underline{\underline{\mathbf{K}}}_e^{\phi_1\phi_1} & \underline{\underline{\mathbf{K}}}_e^{\phi_1\phi_2} \\ \underline{\underline{\mathbf{K}}}_e^{\phi_2 u} & \underline{\underline{\mathbf{K}}}_e^{\phi_2 T} & \underline{\underline{\mathbf{K}}}_e^{\phi_2\phi_1} & \underline{\underline{\mathbf{K}}}_e^{\phi_2\phi_2} \end{bmatrix} \begin{Bmatrix} \Delta\hat{\underline{U}}_e \\ \Delta\hat{\underline{T}}_e \\ \Delta\hat{\underline{\phi}}_{1e} \\ \Delta\hat{\underline{\phi}}_{2e} \end{Bmatrix}, \tag{106}$$

where $\left\{ \underline{\underline{\mathbf{K}}}_e^{uu}, \underline{\underline{\mathbf{K}}}_e^{TT}, \underline{\underline{\mathbf{K}}}_e^{\phi_1\phi_1}, \underline{\underline{\mathbf{K}}}_e^{\phi_2\phi_2} \right\}$ are the tangent stiffness matrices related to the displacement field, thermal field and nonlocal fields, respectively, while the remaining stiffness matrices are related to the coupling between fields. Specifically, the individual stiffness matrices in (106) have the following forms

$$\begin{aligned}
\underline{\underline{\mathbf{K}}}_e^{uu} &= \int_{\Omega_e^0} \left[\underline{\underline{\overline{\mathbf{B}}}}_u^{\mathrm{T}} \underline{\underline{\overline{\boldsymbol{D}}}}_{uu} \underline{\underline{\overline{\mathbf{B}}}}_u + \underline{\underline{\overline{\mathbf{k}}}}_G \right] d\Omega_e^0, \quad \underline{\underline{\mathbf{K}}}_e^{uT} = \int_{\Omega_e^0} \left[\underline{\underline{\overline{\mathbf{B}}}}_u^{\mathrm{T}} \underline{\overline{\boldsymbol{D}}}_{uT} \underline{\boldsymbol{N}} \right] d\Omega_e^0, \\
\underline{\underline{\mathbf{K}}}_e^{u\phi_i} &= \int_{\Omega_e^0} \left[\underline{\underline{\overline{\mathbf{B}}}}_u^{\mathrm{T}} \underline{\overline{\boldsymbol{D}}}_{u\phi_i} \underline{\boldsymbol{N}} \right] d\Omega_e^0, \ i = 1,2, \quad \underline{\underline{\mathbf{K}}}_e^{Tu} = \int_{\Omega_e^0} \left[\underline{\underline{\widetilde{\mathbf{B}}}}_T^{\mathrm{T}} \underline{\underline{\overline{\mathbf{D}}}}_{\mathbf{K}_0} \underline{\underline{\overline{\mathbf{B}}}}_u - \underline{\boldsymbol{N}}^{\mathrm{T}} \underline{\overline{\boldsymbol{D}}}_{Tu} \underline{\underline{\overline{\mathbf{B}}}}_u \right] d\Omega_e^0, \\
\underline{\underline{\mathbf{K}}}_e^{TT} &= \int_{\Omega_e^0} \left[\underline{\boldsymbol{N}}^{\mathrm{T}} \left(\frac{c_0}{\Delta t} - \overline{C}_{TT} \right) \underline{\boldsymbol{N}} + \underline{\underline{\mathbf{B}}}_T^{\mathrm{T}} \underline{\underline{\mathbf{K}}}_0 \underline{\underline{\mathbf{B}}}_T \right] d\Omega_e^0, \quad \underline{\underline{\mathbf{K}}}_e^{T\phi_i} = \int_{\Omega_e^0} \left[\underline{\boldsymbol{N}}^{\mathrm{T}} \overline{C}_{T\phi_i} \underline{\boldsymbol{N}} \right] d\Omega_e^0, \ i = 1,2, \\
\underline{\underline{\mathbf{K}}}_e^{\phi_i u} &= \int_{\Omega_e^0} \left[\underline{\boldsymbol{N}}^{\mathrm{T}} \underline{\overline{\boldsymbol{D}}}_{\phi_i u} \underline{\underline{\overline{\mathbf{B}}}}_u \right] d\Omega_e^0, \ i = 1,2, \quad \underline{\underline{\mathbf{K}}}_e^{\phi_i T} = \int_{\Omega_e^0} \left[\underline{\boldsymbol{N}}^{\mathrm{T}} \overline{C}_{\phi_i T} \underline{\boldsymbol{N}} \right] d\Omega_e^0, \ i = 1,2, \\
\underline{\underline{\mathbf{K}}}_e^{\phi_i\phi_j} &= \int_{\Omega_e^0} \left[\underline{\boldsymbol{N}}^{\mathrm{T}} \left(E\delta_{ij} - \overline{C}_{\phi_i\phi_j} \right) \underline{\boldsymbol{N}} + \delta_{ij} \beta \underline{\underline{\mathbf{B}}}_\phi^{\mathrm{T}} \underline{\underline{\mathbf{B}}}_\phi \right] d\Omega_e^0, \ i,j = 1,2,
\end{aligned} \tag{107}$$

where $\underline{\underline{\overline{\mathbf{D}}}}_{uu}$ is the 6×6 matrix form of the fourth order tensor $\overline{\mathbb{C}}_{uu}$. $\underline{\overline{\boldsymbol{D}}}_{uT}$ and $\underline{\overline{\boldsymbol{D}}}_{u\phi_i}$ are the 6×1 vector forms of the second order tensors $\overline{\mathbf{C}}_{uT}$ and $\overline{\mathbf{C}}_{u\phi_i}$, respectively. $\underline{\underline{\overline{\mathbf{D}}}}_{\mathbf{K}_0}$ is the 6×6 matrix form of the fourth order tensor $\overline{\mathbb{C}}_{\mathbf{K}_0}$. $\underline{\overline{\boldsymbol{D}}}_{Tu}$ and $\underline{\overline{\boldsymbol{D}}}_{\phi_i u}$ are the vector form of 1×6 of the second order tensors $\overline{\mathbf{C}}_{Tu}$ and $\overline{\mathbf{C}}_{\phi_i u}$, respectively. The geometric tangent stiffness matrix per unit volume, $\underline{\underline{\overline{\mathbf{k}}}}_G$, is defined by

$$\overline{\mathbf{S}} : \Delta\delta\overline{\mathbf{E}} = \delta\hat{\underline{U}}_e^{\mathrm{T}} \underline{\underline{\overline{\mathbf{k}}}}_G \Delta\hat{\underline{U}}_e, \quad \underline{\underline{\overline{\mathbf{k}}}}_G = \sum_{i=1}^{3} \sum_{j=1}^{3} \overline{S}_{ij} \frac{\partial^2 \overline{E}_{ij}}{\partial\delta\hat{\underline{U}}_e \Delta\hat{\underline{U}}_e}. \tag{108}$$

The details of its derivation are presented in Appendix C. Furthermore, $\underline{\underline{\widetilde{\mathbf{B}}}}_T = \left[\underline{\widetilde{\mathbf{B}}}_{T1}, \ldots, \underline{\widetilde{\mathbf{B}}}_{TN_{en}} \right]$ groups all the $\underline{\widetilde{\mathbf{B}}}_{TI}$ vectors which are given by

$$\underline{\widetilde{\mathbf{B}}}_{TI} = \left\{ \frac{\partial T}{\partial X_1} N_{I,1} \quad \frac{\partial T}{\partial X_2} N_{I,2} \quad \frac{\partial T}{\partial X_3} N_{I,3} \quad \frac{\partial T}{\partial X_1} N_{I,2} + \frac{\partial T}{\partial X_2} N_{I,1} \quad \frac{\partial T}{\partial X_1} N_{I,3} + \frac{\partial T}{\partial X_3} N_{I,1} \quad \frac{\partial T}{\partial X_2} N_{I,3} + \frac{\partial T}{\partial X_3} N_{I,2} \right\}^{\mathrm{T}}. \tag{109}$$

Based on the foregoing derivations, a user-defined element subroutine UEL is developed in ABAQUS to compute the internal force vectors (105), and the element stiffness matrices (107). The integrals are evaluated by means of numerical integration over the element domain. In the present three-dimensional solid element formulation, a standard $2 \times 2 \times 2$ Gauss integration scheme with trilinear shape functions is adopted.

One major bottleneck in computational inelasticity is the computation of internal variables. To circumvent this challenge, we employ the analytical inelasticity framework developed in [16,38,41,42,53], which provides direct analytical expressions for the internal variables (33). As illustrated in Fig. 4, the computational cost is drastically reduced compared to the classical predictor–corrector approach. A full Newton–Raphson strategy is employed throughout all simulations in this work. No additional globalization techniques, such as line search or damping, are required to ensure numerical stability. For time integration, a backward Euler scheme combined with an adaptive time-stepping strategy is adopted to improve computational efficiency. The adaptive procedure automatically adjusts the time increment according to the convergence behavior of each increment: larger time steps are used when convergence is achieved rapidly, whereas smaller time steps are introduced when the material response becomes highly

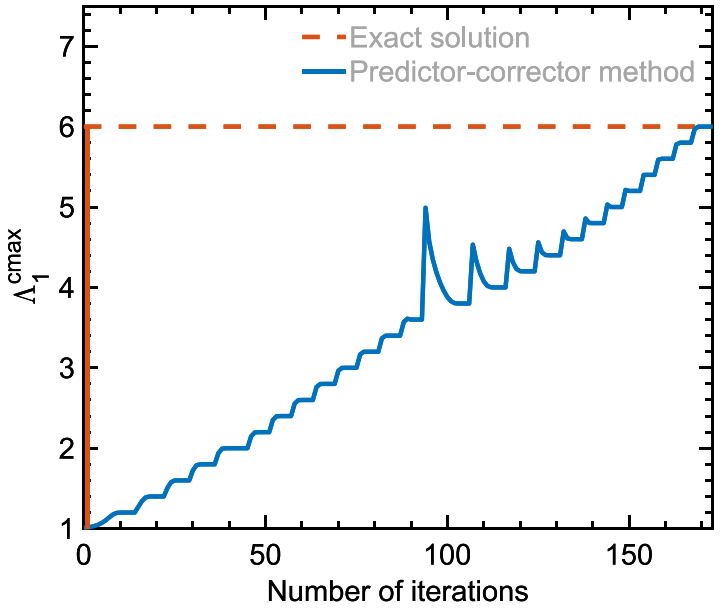


Fig. 4. Comparison between analytical and numerical solutions of the internal variable $\Lambda_1^{c\,max}$ at $\phi_1 = 5$. While the analytical solution obtains the exact result directly, the numerical solution requires 170 iterations to achieve the same result. The material parameters given in Table 1 are used for this numerical example.

Table 3
Convergence criteria used in the Newton–Raphson iterations [56].

Criterion	Tolerance
Ratio of the largest residual to the corresponding average values	5.0×10^{-3}
Ratio of the largest solution correction to the largest corresponding incremental solution values	1.0×10^{-2}

Table 4
Physical meaning of the material constants.

Parameters	Physical meaning
$\mu_{c0} = N_{c0} k_B T_0 \kappa$	Effective phantom shear modulus at the room temperature [MPa]
n	Average number of chain segments
$\mu_{t0} = N_{c0} k_B T_0 \omega$	Topological shear modulus at the room temperature [MPa]
B_1	Primary crystallinity constant
B_2	Secondary crystallinity constant
k_B	Boltzmann's constant 1.380649e−20 $[\frac{mJ}{K}]$
T_0	Initial temperature [K]
$\gamma_t \gamma_s^2$	Surface tension product $[\frac{mJ^3}{mm^6}]$
$\check{\chi}$	Relative ratio of surface tension for secondary formation
$\hat{\chi}$	Relative ratio of surface tension for secondary melting
q_0	Stretch amplification exponent
$\mathcal{K}$	Bulk modulus [MPa]
E	Young modulus of molecular bond 1e6 [MPa]
β	Nonlocal interaction permittivity 1 [N]
c_0	Heat capacity per unit volume 1.645 $[\frac{mJ}{mm^3\,K}]$
k	Thermal conductivity 0.146 $[\frac{mW}{mm\,K}]$
Δh	Latent heat of fusion 64.015 $[\frac{mJ}{mm^3}]$

nonlinear. For a loading duration of 13 [s], the time increment varies from 0.005 [s] to 0.25 [s]. Typically, convergence is achieved within 3–6 Newton iterations per increment. Furthermore, no convergence difficulties are observed near the onset of strain-induced crystallization. The convergence criteria employed in the simulations are summarized in Table 3.

7. Results

For ease of reference, Table 4 summarizes all parameters used in the computational framework and their physical meanings. In all numerical examples, the nonlocal parameters E, β, and thermal parameters T_0, k, Δh, and c_0 are fixed at the values listed

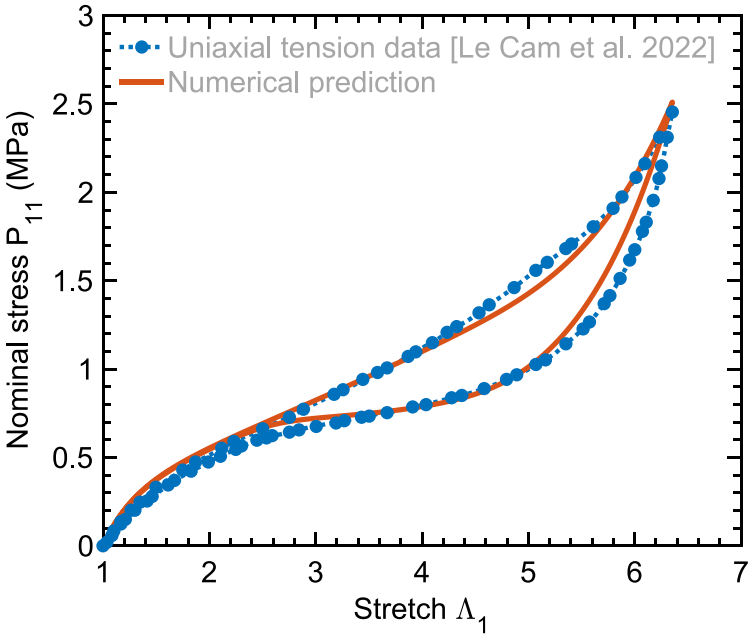


Fig. 5. Average nominal stress in the uniaxial tension experiment.

in Table 4. The remaining mechanical parameters are identified by fitting the model to experimental data using the Levenberg–Marquardt algorithm, where the objective function is defined in terms of the squared error between the measured quantities and the corresponding model predictions.

7.1. Tension of unfilled natural rubber

In this section, we investigate the heterogeneity of temperature and crystallinity in unfilled natural rubber during homogeneous uniaxial tension and compare the numerical predictions with experimental results obtained via quantitative surface calorimetry. The details on material and experimental technique are described in Appendix A. A rectangular sample of dimension $12 \times 9.64 \times 2$ mm is clamped at its lower edge and stretched vertically to a global stretch ratio of 6.35 at a displacement rate 5 $[\frac{\text{mm}}{s}]$. The corresponding numerical sample is then discretized by 1920 brick elements. Convection boundary condition is applied on the outer surface of the specimen with a film coefficient of $0.011136\,[\frac{\text{mW}}{\text{mm}^2\,\text{K}}]$ and a far field temperature $293\,[\text{K}]$. To mimic the intrinsic heterogeneous distribution of cross-link densities in natural rubbers, randomly distributed initial shear moduli are introduced into the finite element model. Material constants for the local part are given in Table 1, whereas nonlocal and temperature field related parameters are given in Table 4. The average nominal stress, calculated from the ratio of force and initial cross-sectional area, is demonstrated in Fig. 5. It can be seen that due to regularization, there is no stress plateau observed after the onset of SIC in Fig. 5 (cf. Fig. 2a).

7.1.1. Temperature variation on the sample surface

Temperature distribution predicted by the computational framework is plotted on Fig. 6. It is observed that before the onset of SIC, the temperature field is homogeneous, however around stretch 4.5–5.3, the temperature field is highly inhomogeneous, indicating the loss of ellipticity in the local model as analyzed in Fig. 2*b*. When the extension exceeds the stretch ratio 5.3, the temperature field becomes homogeneous again. Since the temperature heterogeneity occurs only within the stretch domain in which the theoretical framework predicts loss of ellipticity, we argue that the two phenomena are intrinsically connected. If the temperature heterogeneity were solely caused by a pre-existing heterogeneous microstructure, there would be no obvious reason for it to appear only within this particular stretch range while remaining absent outside it. On the other hand, the distribution of temperature field is always homogeneous in non-crystallizing rubbers (by setting $\gamma_1\gamma_s^2 \to \infty$). From our perspective, the temperature heterogeneity originates from the loss of ellipticity due to SIC, however, it can only be captured numerically when imperfections (such as crosslink density heterogeneity) are taken into account. It cannot be attributed solely to crosslink density heterogeneity, as neither temperature nor crystallinity heterogeneity is numerically observed in noncrystallizing materials with randomly distributed shear modulus.

Furthermore, crystallization degree is also observed to be inhomogeneously distributed across the specimen within the same deformation range (Fig. 7). However, since the magnitude of crystallization degree does not directly quantify the loss of ellipticity, temperature provides a more reliable indicator, owing to its direct coupling to the stress field through the diffusion–convection Eq. (57).

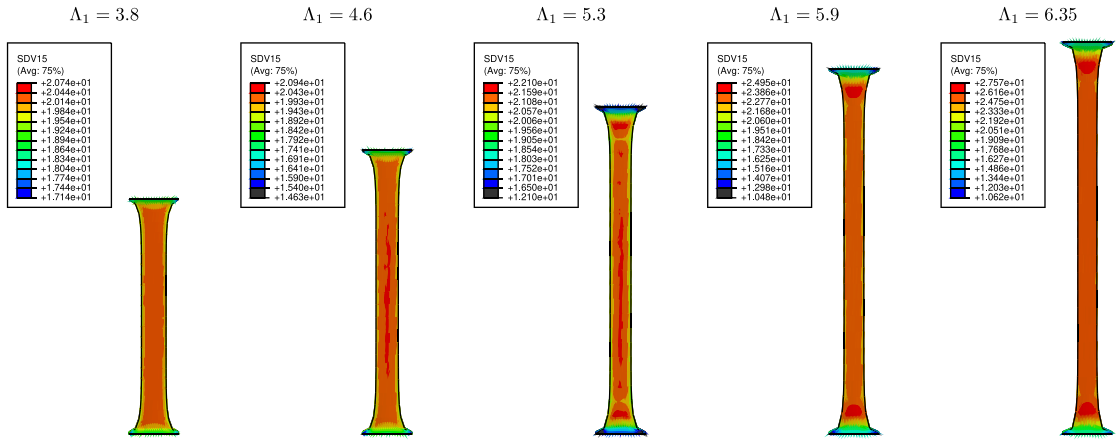


Fig. 6. Heterogeneity of temperature distribution after the onset of SIC ($\Lambda_1 = 4.5 - 5.3$) in a homogeneous uniaxial tension of unfilled natural rubber due to the loss of ellipticity.

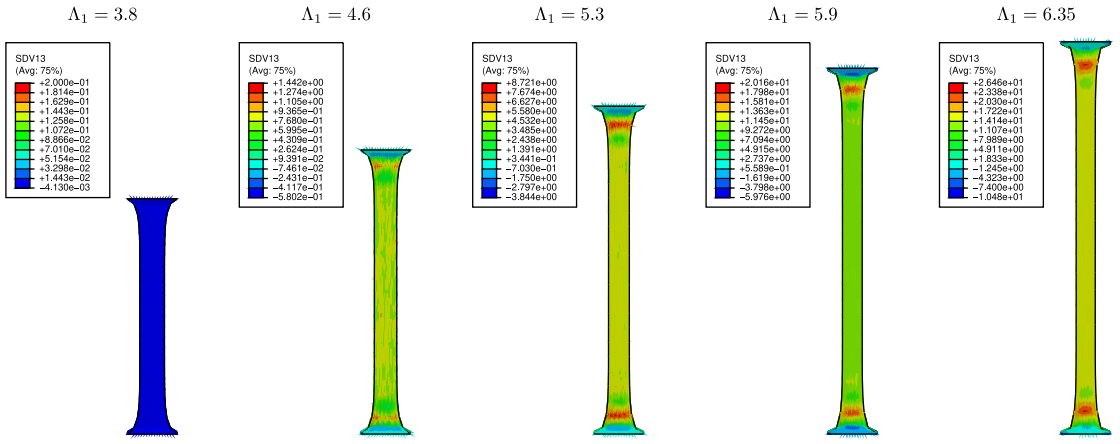


Fig. 7. Heterogeneity of crystallization degree after the onset of SIC ($\Lambda_1 = 4.5 - 5.3$) in a homogeneous uniaxial tension of unfilled natural rubber due to the loss of ellipticity.

Table 5
Heat production and absorption predicted at the center of the specimen during cyclic loading of unfilled natural rubber.

Computed quantities	$\Lambda_1 = 4.5$	$\Lambda_1 = 5.5$	$\Lambda_1 = 6.35$
Heat production (under loading) $[\frac{\text{MW}}{\text{m}^3}]$	1.275	3.285	6.193
Heat absorption (under unloading) $[\frac{\text{MW}}{\text{m}^3}]$	1.275	3.286	6.201

7.1.2. Local predictions of crystallinity and heat source

The predicted heat source (62) at the center of the specimen is then plotted versus time in Fig. 8. It can be observed that, initially, the heat source increases with crystallinity. Near the end of the loading phase, the heat source decreases due to the inflection point in the evolution of crystallinity, as observed in the predicted heat supply $\widehat{R} = \Delta h \dot{\zeta}$ (Fig. 8). However, since the model overestimates the stress power (Fig. 5), this reduction is diminished in the numerical heat source. Furthermore, to investigate internal dissipation in unfilled natural rubber, the heat sources predicted over three loading cycles are shown in Fig. 9. As reported in Table 5, the heat production (area under the heat source during loading) and the heat absorption (area above the heat source during unloading) are identical at all deformation levels, indicating zero internal dissipation [15,16].

Crystallinities along the middle section of the sample are then compared with 12 experimentally measured points in Fig. 10. Due to randomly distributed cross-link densities, exact nodal values of crystallinity cannot be reproduced. Nevertheless, the evolution of crystallinity agrees well with experimental results at the center of the specimen (Fig. 11).

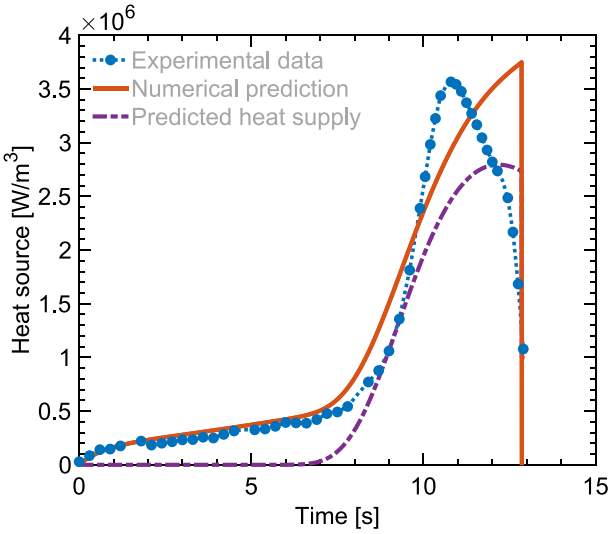


Fig. 8. Heat source (62) and heat supply evolution at the center of the specimen. Time zero is defined as the beginning of the stabilized loading cycle in the experiment.

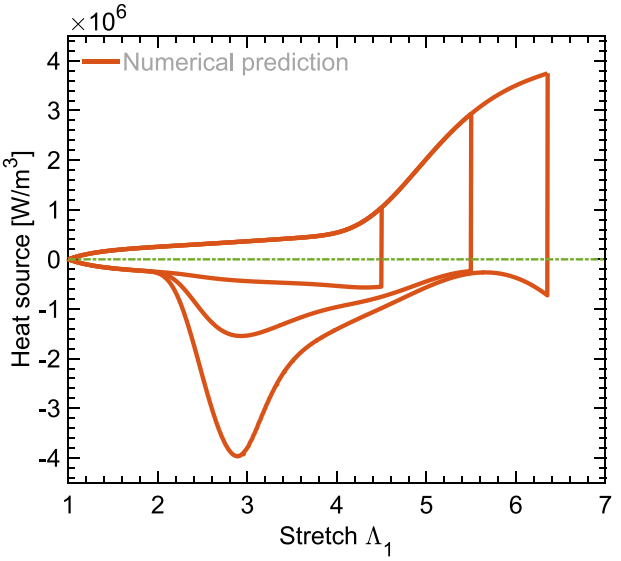


Fig. 9. Heat source predicted at the center of the specimen during three loading cycles with $\Lambda_1 = 4.5, 5.5$ and 6.35.

Table 6
Material constants of the model for the quantitative convergence study.

μ_{c0} [MPa]	n	q_0	μ_{t0} [MPa]	B_1	B_2	$\gamma_t\gamma_s^2$ [$\frac{mJ^3}{mm^6}$]	$\bar{\chi}$	$\mathcal{K}$ [MPa]	E [MPa]	β [N]
0.1813	81	1.0373	0.6	0.32754	0.45301	$3.84e^{-19}$	4.9565	1	2	0.5

7.2. Inhomogeneous deformation of a three-dimensional body

To quantitatively assess the convergence behavior of the proposed computational framework, a numerical experiment on an inhomogeneous deformation of a cubic body of dimension $1 \times 1 \times 1$ mm (Fig. 12*a*) is carried out. The boundary conditions and source terms appearing in (56)–(59) are derived from the prescribed analytical fields together with the material parameters listed

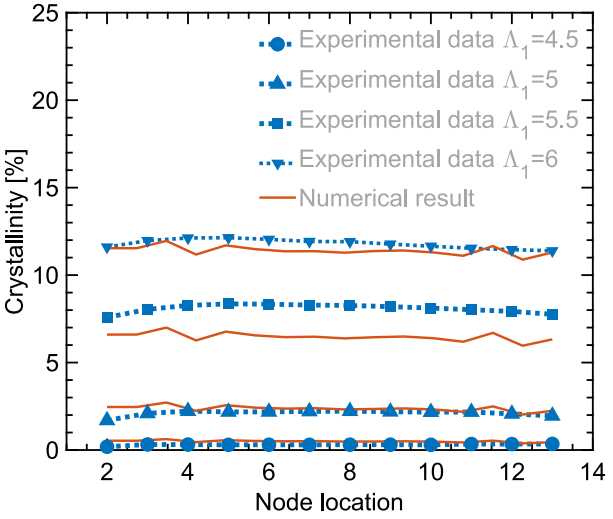


Fig. 10. Distribution of the crystallization degree along the middle cross section of the specimen at different stretch ratios in loading.

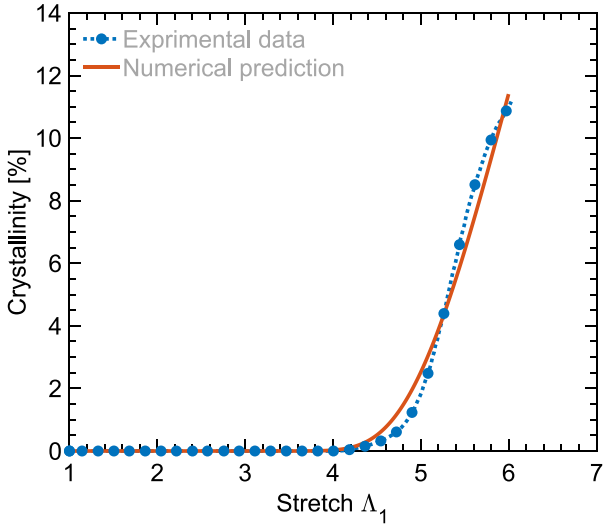


Fig. 11. Crystallinity evolution at the center of the specimen.

in Table 6

$$\boldsymbol{u}^{\text{exact}} = \begin{Bmatrix} A\,X_1^3 t \\ B\,X_2^3 t \\ C\,X_3^3 t \end{Bmatrix}; \quad \boldsymbol{\phi}^{\text{exact}} = \begin{Bmatrix} D\,X_1^3 t \\ F\,X_2^3 t \end{Bmatrix}; \quad T^{\text{exact}} = \left(G\,X_1^3 + T_0\right)(H\,t + 1), \tag{110}$$

where A, B, C, D, F, G and H are constants provided in Table 7. By applying the boundary conditions and source terms, the convergence of all field variables to their exact solutions can be systematically evaluated. For that purpose, the L_2-norm errors of the numerical solutions with respect to the exact solutions are computed for a sequence of progressively refined meshes (Fig. 12*b*).

As expected, the results demonstrate second-order mesh convergence for all field variables within the proposed computational framework using linear finite element. The near-optimal convergence in temperature field can be attributed to the backward Euler time integration scheme, whose temporal discretization error is first-order in the time increment. This limitation will be addressed in future work through the implementation of higher-order time integration schemes. Furthermore, the quadratic convergence rate

Table 7
Constants of the exact field variables.

$A\left[\frac{1}{\text{s mm}^2}\right]$	$B\left[\frac{1}{\text{s mm}^2}\right]$	$C\left[\frac{1}{\text{s mm}^2}\right]$	$D\left[\frac{1}{\text{s}}\right]$	$F\left[\frac{1}{\text{s}}\right]$	$G\left[\frac{\text{K}}{\text{mm}^3}\right]$	$H\left[\frac{1}{\text{s}}\right]$
1.6	0.2	0.1	7	5	2	0.5

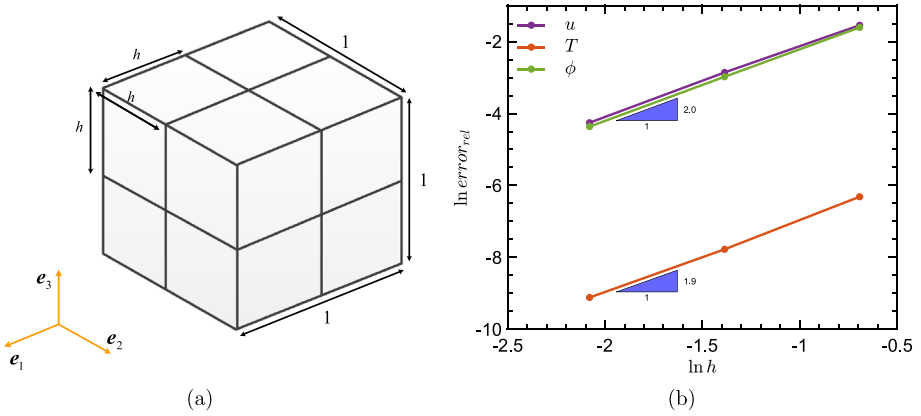


Fig. 12. Quantitative convergence study of the proposed formulation: (a) Sample geometry, and (b) Order of accuracy of different field variables. The relative error is defined as the ratio of the mean error to the mean value of the corresponding field over the entire material body.

of the Newton–Raphson solver is illustrated in Fig. 13. Note that the maximum value of ϕ is significantly greater than 3 (Table 7 and $(110)_2$), indicating that the deformation state is well beyond the onset of strain-induced crystallization. Therefore, the phase transition affects neither the mesh convergence nor the solver convergence of the current framework.

7.3. Deformation of a cylindrical bar

To analyze the physical interpretation and mesh-objectivity of the regularized solution, we consider the tension of a cylindrical bar with a length of 60 [mm] and a radius of 10 [mm], subject to adiabatic thermal boundary conditions. Owing to symmetry, only one quarter of the specimen is modeled, with symmetric boundary conditions applied at the mid-plane of the bar and along the symmetry planes. The domain is discretized using an $n\times 3n$ finite element mesh. A vertical displacement of 60 [mm] is prescribed at the top surface of the bar, while a lateral displacement of -2.5 [mm] is imposed along the line 20 [mm] below the top surface (Fig. 14*a*). The material parameters given in Table 1 are used for this numerical example. The results show that the nonlocal variable exceeds a value of 4, corresponding to stretches greater than 5. No convergence difficulties are observed after the onset of strain-induced crystallization. A mesh refinement study demonstrates that the regularized solution is mesh-objective, with convergence achieved for $n = 32$ (Fig. 14*b*).

A sensitivity analysis of the nonlocal interaction parameter β was conducted for values of β ranging from 10^{-4} [N] to 10^{12} [N]. As shown in Fig. 15, when $\beta \geq 10^4$ [N], the width of the nonlocal band (measured as the region where $\phi_1^{\max}$ is spatially nonuniform) increases with increasing β. When $\beta < 10^4$ [N], no significant change in the width of the nonlocal band is observed. When $\beta > 10^{12}$ [N], the width of the nonlocal band becomes infinite. Such observation fully aligns with the physical interpretation of the parameter β as the permittivity of nonlocal interaction. As β increases, the strength of the nonlocal interactions increases, allowing the nonlocal interaction field to spread over a larger region of the polymer.

Furthermore, we compare the internal dissipation predicted by our framework with that obtained from a gradient damage (or phase-field [55]) model, in which the internal variables ϕ_1^{int} and ϕ_2^{int} are defined via

$$E\varepsilon_1^{\max} = E\phi_1^{\text{int}} - \text{Div}\left(\beta \text{Grad}\phi_1^{\text{int}}\right), \tag{111}$$

$$E\varepsilon_2^{\max} = E\phi_2^{\text{int}} - \text{Div}\left(\beta \text{Grad}\phi_2^{\text{int}}\right). \tag{112}$$

The results (Fig. 16) clearly show that the internal dissipation in our framework remains identically zero for crystallizing polymers, whereas the gradient-damage (or phase-field) model exhibits both positive and negative dissipation values at different locations within the mesh. This indicates that the gradient-damage (or phase-field) model is not strictly thermodynamically consistent.

7.4. Cook's membrane problem

With this numerical example, we validate the convergence behavior of the finite element formulation in the Cook's membrane test. To this end, we consider a trapezoidal panel 2 mm thick, fixed on the left side and subjected to uniform displacement on the right side (Fig. 17*a*). The panel is discretized by $4n \times 4n \times 2n$ elements. Material parameters of the model are given in Table 8.

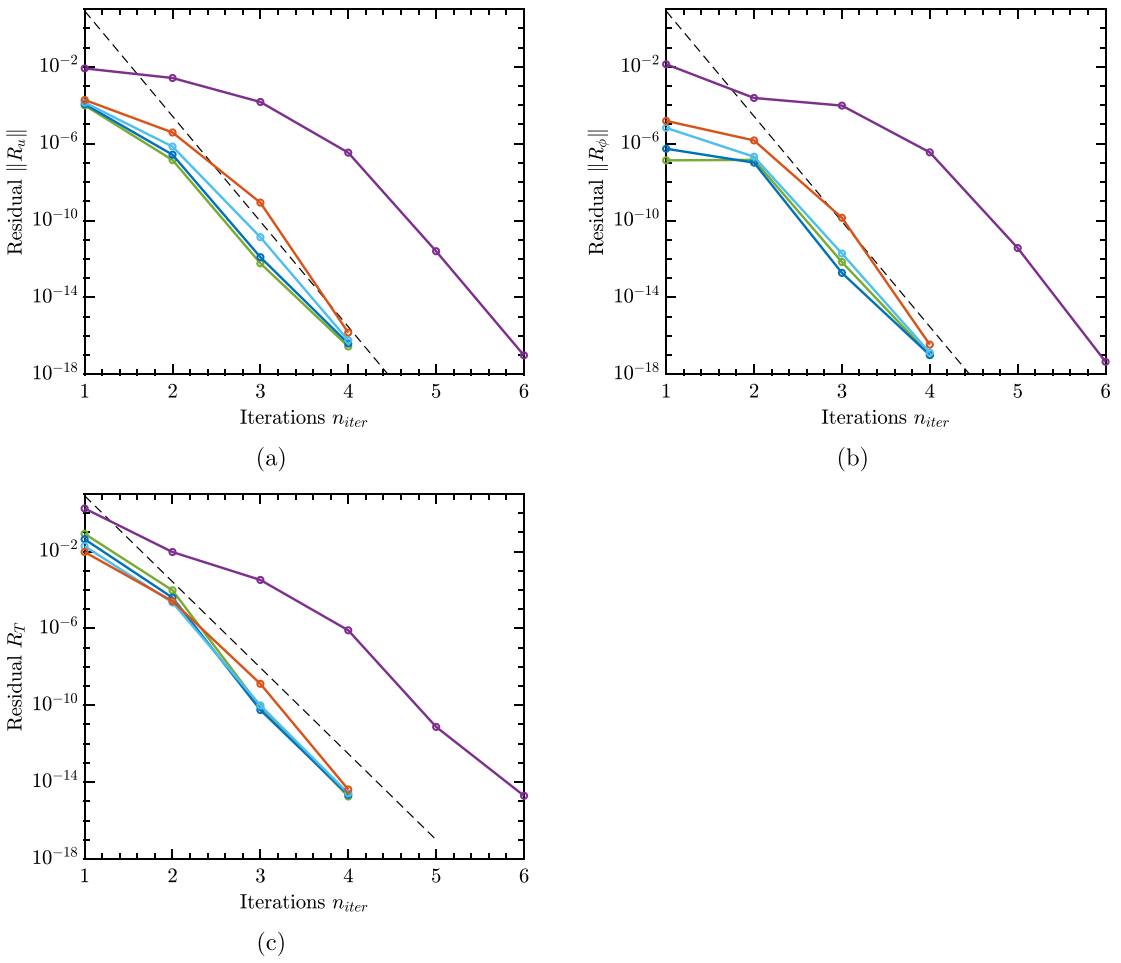


Fig. 13. Rate of convergence of the residual norms associated with: (a) displacement $\|\boldsymbol{R}_u\|$, (b) nonlocal variables $\|\boldsymbol{R}_\phi\|$, and (c) temperature R_T, with respect to the number of iterations. The dashed lines $-\frac{\log \Delta R}{\Delta n_{iter}} = 2$ are included as references for quadratic convergence.

Table 8
Material constants of the proposed model for the example in Section 7.4.

μ_{c0}	n	q_0	μ_{t0}	B_1	B_2	$\gamma_t \gamma_s^2$ [$\frac{\text{mJ}^3}{\text{mm}^6}$]	$\tilde{\chi} = \hat{\chi}$	T_0	$\mathcal{K}$
0.182	52.2741	1.0573	1.0361	0.2831	0.4359	$2.4988e^{-19}$	1.9209	293	200

Convection boundary condition is applied on the outer surface of the specimen with a film coefficient of $0.0174\,[\frac{\text{mW}}{\text{mm}^2\ \text{K}}]$ and a far field temperature $293\,[\text{K}]$. Reaction force on the right side is plotted in Fig. 17*b* for different discretizations. It can be observed that the reaction force values are identical for $n = 5, 6, 7, 8$. Thus, converged solution is reached for the mesh size with $n \geq 5$.

7.5. Planar biaxial tension experiment

In this section, we consider a planar biaxial tension of unfilled natural rubber sample [57,59]. Accordingly, the square specimen is extended with different stretch ratios (Λ_1, Λ_2) along two orthogonal directions (Fig. 18*a*) to investigate the evolution of crystallinity associated with variations in the biaxiality ratio $\gamma = \log_{\Lambda_1} \Lambda_2$ (Fig. 18*b*).

According to our theory, an increase in the biaxiality ratio enhances the second term of (4), thereby reducing the free energy change associated with the deformation of oriented polymer strands. This reduction increases the energy barrier for crystal nucleation (3), making crystallite formation in unfilled natural rubbers more difficult under biaxial tension than under uniaxial tension (Fig. 18*c*). One can observe very good agreement between theoretical prediction (Fig. 18*d*) with the material parameters given in Table 9 and experimental results (Fig. 18*b*). For constructing the maps in Fig. 18*c*, *d*, the energy barrier and crystallinity were evaluated on a regular 1024×1024 grid of deformation states.

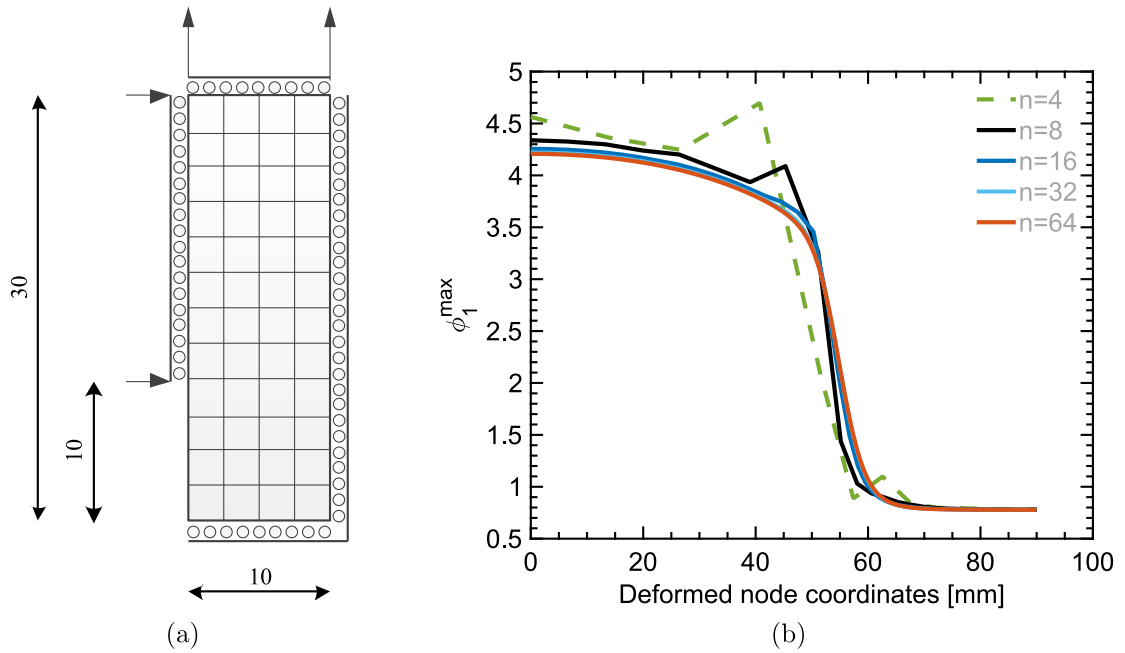


Fig. 14. Numerical example with nonlocal band, the origin of the coordinate system is located at the center of symmetry: (a) Boundary condition and (b) Mesh-objectivity of the regularized solution. The convergence reaches at $n = 32$.

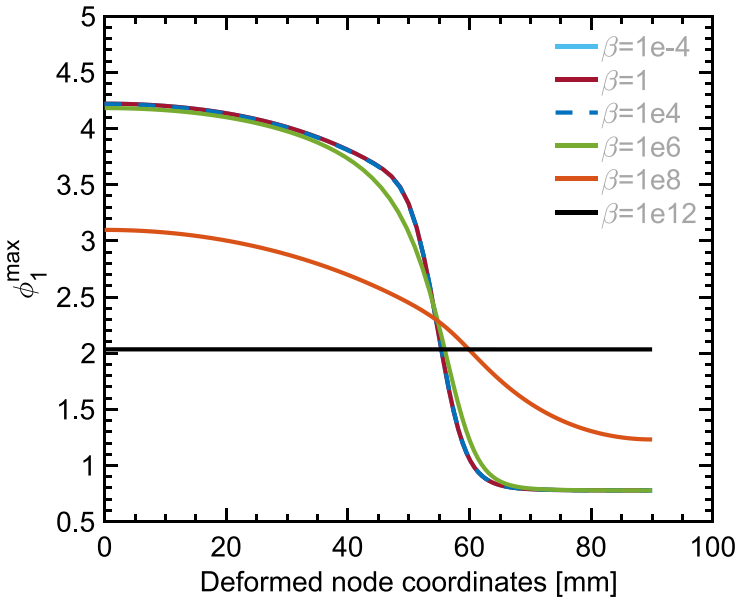


Fig. 15. Sensitivity analysis of the nonlocal interaction parameter.

Furthermore, a detailed comparison between the predicted crystallinity during a sequential loading (constrained tension at $\Lambda_2 = 1$, followed by constrained tension at $\Lambda_1 = 5$, Fig. 19*a*) and the experimental measurements [57] is shown in Fig. 19*b*. As

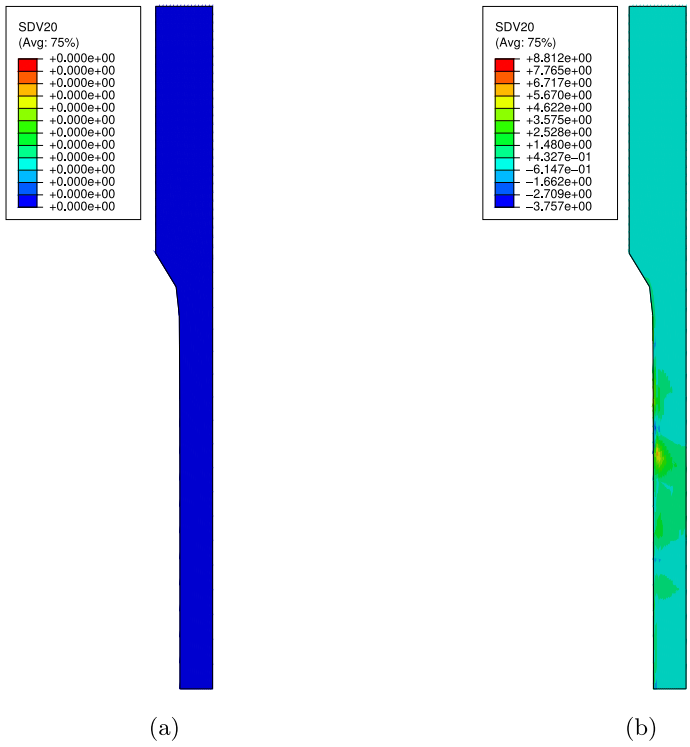


Fig. 16. Internal dissipation predicted by different methods: (a) In the thermodynamic regularization approach, the internal dissipation of unfilled natural rubber is always zero, which is consistent with experimental observations [15]. (b) In the gradient damage (or phase-field [55]) approach, the internal dissipation $-\sum_{i=1}^{2} \frac{\partial \Psi}{\partial \phi_i^{\text{int}}} \dot{\phi}_i^{\text{int}}$ can become either positive or negative. This implies that these frameworks are thermodynamically inconsistent and in contradiction with experimental observations of natural rubbers.

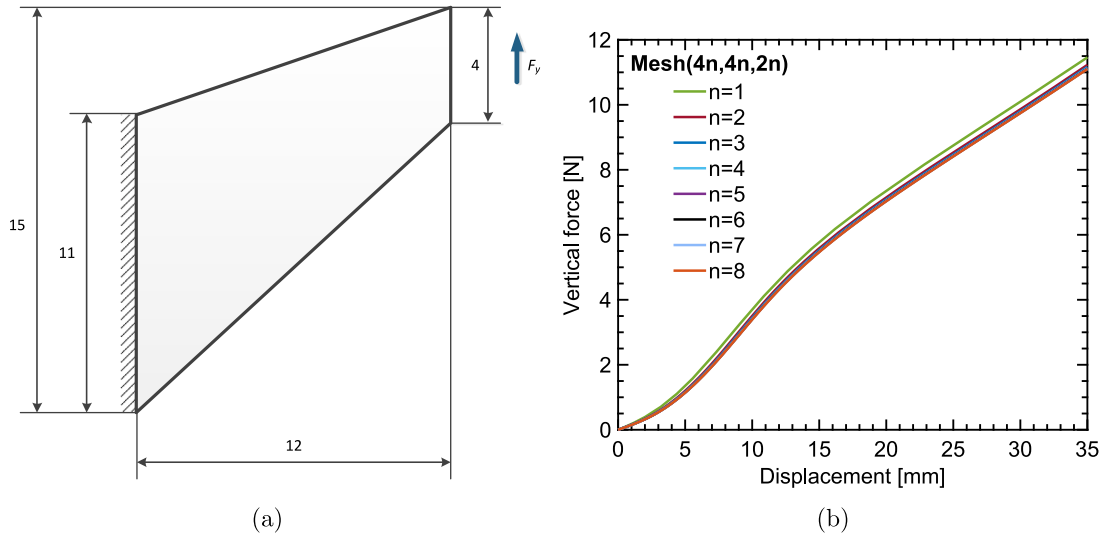


Fig. 17. Cook's membrane benchmark case: (a) Sample geometry and boundary conditions, and (b) Force–displacement predicted by different discretizations.

expected, the crystallinity decreases immediately when the loading state changes from pure shear to biaxial tension. To the best of our knowledge, none of the previously proposed theoretical models can explain such experimental observation.

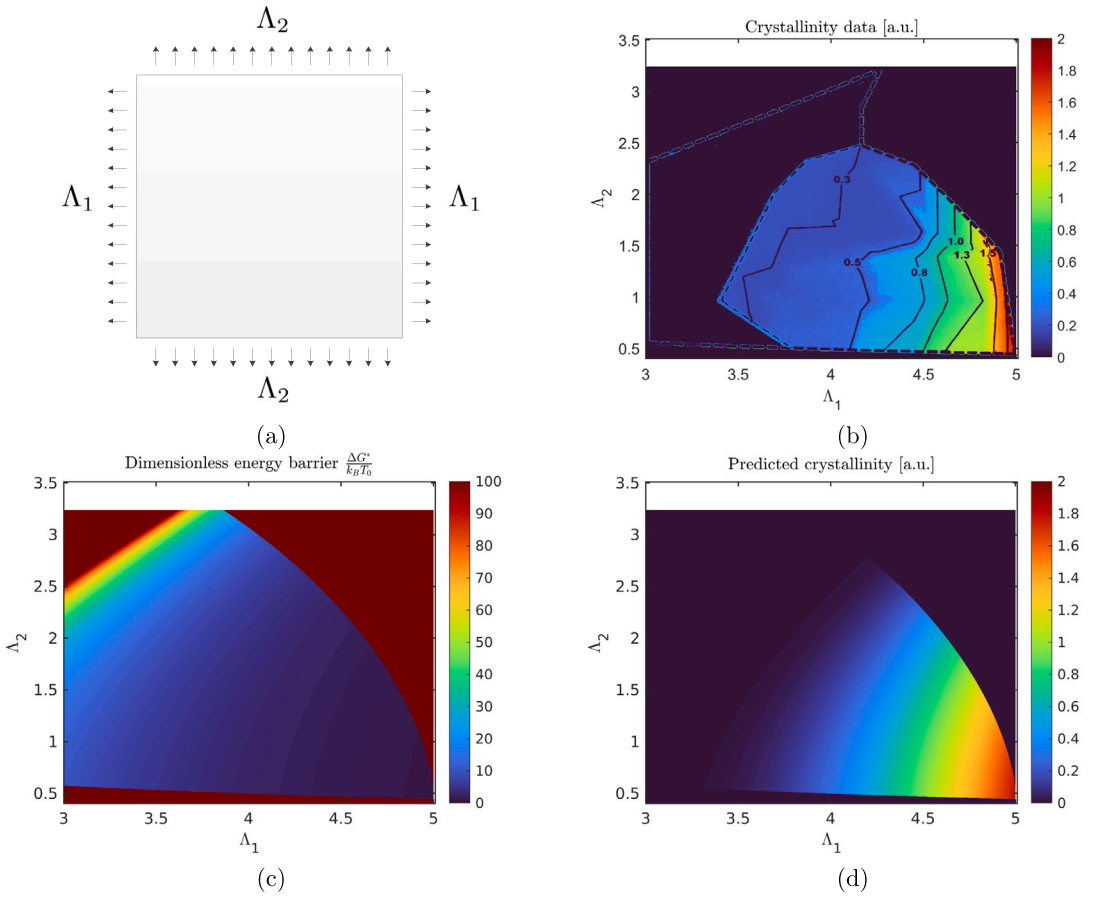


Fig. 18. Change in crystallinity [a.u.] under biaxial tension: (a) Boundary conditions; (b) Experimental data of crystallinity versus principal stretches Λ_1 and Λ_2 [57], where the biaxiality ratio γ increases from -0.5 (lower region) to 1 (upper region); (c) Theoretical prediction of energy barrier for crystal nucleation; and (d) Numerical prediction, the zero-crystallinity regions in the lower and upper-right areas arise from inadmissible stretches, corresponding respectively to deformation outside the experimentally explored range and to stretches at the subnetwork level [40,58] exceeding the limit of extensibility 2.9445.

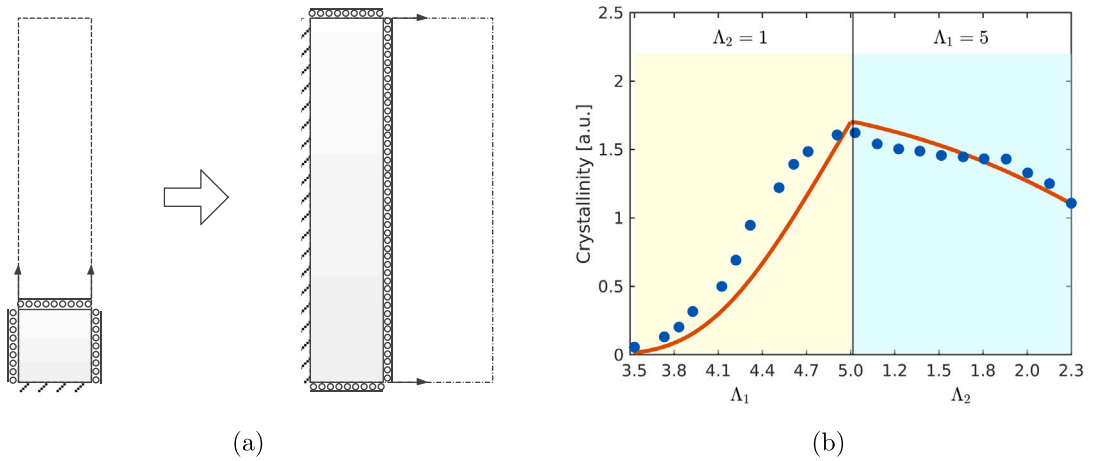


Fig. 19. Evolution of crystallinity during sequential constrained tension: (a) Boundary conditions, and (b) Crystallinity versus stretch: filled circles indicate experimental data [57], while the solid line shows the model prediction.

Table 9
Material constants of the proposed model for the example in Section 7.5.

μ_{c0} [MPa]	n	q_0	μ_{t0} [MPa]	B_1 [a.u.]	B_2 [a.u.]	$\gamma_t\gamma_s^2$ [$\frac{mJ^3}{mm^6}$]	$\bar{\chi} = \hat{\chi}$	T_0	$\mathcal{K}$
0.1648	66	1.9604	0.5455	4.9051	7.5708	$9.9616e^{-20}$	1.3534	294	1e4

8. Conclusion

On the basis of thermodynamic regularization [38], we developed in this paper a nonlocal, physically grounded computational framework to tackle the breakdown of ellipticity in deformation-induced phase transition of natural rubbers. Within this framework, the free-energy function of natural rubber consists of both local and nonlocal contributions. The local free energy arises from a generalization of a uniaxial theoretical formulation [16], enabling predictions under arbitrary states of deformation. Nonlocal interactions within the polymer network were modeled as electric fields, with their range of influence controlled by a permittivity parameter. Furthermore, the governing equations for the nonlocal fields were derived from the laws of thermodynamics, thereby preserving the physical interpretation of the nonlocal parameters. The framework was validated against sophisticated experimental data of unfilled natural rubbers and provides a satisfactory explanation of experimental observations. For example, the heterogeneous temperature distribution observed under macroscopically homogeneous deformation is attributed to loss of ellipticity, while the reduction of strain-induced crystallinity under biaxial loading arises from a decrease in the free-energy change associated with oriented polymer strands. These results highlight the enduring power of continuum mechanics domain knowledge in the age of data science and underscore the importance of high-quality experimental data for uncovering nontrivial physical insights.

CRediT authorship contribution statement

Mahmood Jabareen: Writing – review & editing, Writing – original draft, Validation, Supervision, Software, Methodology, Conceptualization. **Vu Nguyen-Xuân:** Writing – review & editing, Visualization, Software, Investigation, Formal analysis. **Mikhail Itskov:** Writing – review & editing, Supervision, Resources, Project administration. **Jean-Benoît Le Cam:** Writing – review & editing, Validation, Data curation. **Vu Ngoc Khiêm:** Writing – review & editing, Writing – original draft, Visualization, Validation, Supervision, Software, Resources, Project administration, Methodology, Investigation, Funding acquisition, Formal analysis, Data curation, Conceptualization.

Declaration of competing interest

The authors declare that they have no known competing financial interests or personal relationships that could have appeared to influence the work reported in this paper.

Acknowledgments

V.N. Khiêm and M. Itskov gratefully acknowledge the German Research Foundation (DFG) for the financial support of this work (Project number 492017525 and 500476685, respectively). Also, M. Jabareen is supported by Neubauer Foundation.

Appendix A. Calorimetric analysis

A.1. Material

The experiment is carried out with a rectangular sample of unfilled NR1.2 [21]. Fig. A.20 presents an overview of the experimental setup composed of a uniaxial testing machine, an infrared camera, and the rectangular specimen.

A.2. Quantitative surface calorimetry

Quantitative surface calorimetry involves the identification of the heat source through temperature field measurement, employing the heat diffusion equation. The temperature field, measured using an infrared camera on the flat surface of the sample, is inherently two-dimensional. Thus, the three-dimensional heat diffusion equation (42) must be adapted to this scenario through a series of assumptions. First, heat conduction is treated as isotropic. Second, the material is considered incompressible, $\det \mathbf{F} = 1$, cf. (42). Third, the temperature is assumed to remain constant along the specimen's thickness, which can be justified for a relatively thin specimen. As a result, the left hand side of (42) can be integrated over the thickness as

$$\rho_0 c \left(\dot{\theta} + \frac{\theta}{\tau_{2D}} \right) - \mathrm{Div}_{2D}(k\mathbf{C}^{-1}\mathrm{Grad}_{2D}\theta) = \hat{S}, \tag{A.1}$$

where $\hat{S}$ denotes the heat source, and the temperature variation $\theta(X,Y,t) = T(X,Y,t) - T_{ref}(X,Y)$ is introduced to eliminate the effect of constant external radiation from the heat diffusion equation. In the absence of external radiation, the ambient temperature

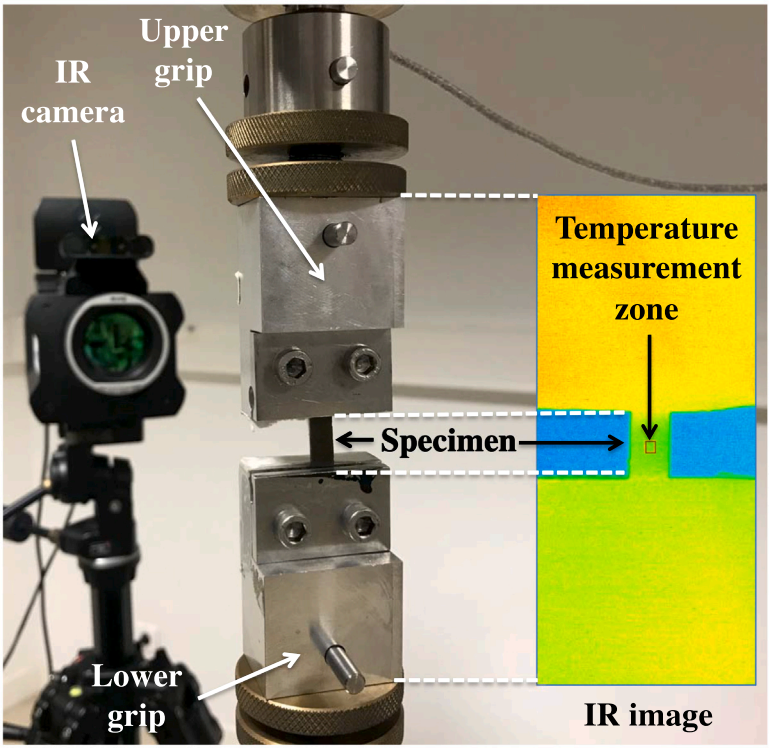


Fig. A.20. Overview of the experimental setup.

T_{amb} remains constant throughout the experiment, so that $T_{ref} = T_{amb}$. Furthermore, τ_{2D} is a characteristic time of heat exchanges along the thickness direction, due to convection with the surrounding air at the specimen surface.

Since the thermal diffusivity of natural rubbers is low, the thermal gradient is localized mainly within the vicinity of the grips of the test machine. Consequently, when the heat conduction within the specimen plane is negligible, the two-dimensional heat diffusion equation can be further reduced to [60–62]

$$\rho_0 c \left(\dot{\theta} + \frac{\theta}{\tau}\right) = \widehat{S}, \tag{A.2}$$

where τ represents the characteristic time of a natural return to room temperature after heating (or cooling) for each testing configuration [2]. Consequently, the heat source $\widehat{S}$ is fully determined.

Appendix B. Derivatives of the primary and secondary crystallinities

With the primary crystallinity defined in (2), the first and second derivatives of the primary crystallinity with respect to the nonlocal variables ϕ_1 and ϕ_2 are given by

$$\begin{aligned}
\frac{\partial \zeta_{\mathrm{I}}}{\partial \phi_i} &= 2\frac{\zeta_{\mathrm{I}}}{k_{\mathrm{B}}T_0}\frac{\Delta G^*\left(\phi_1,\phi_2\right)}{\Delta \Psi\left(\phi_1,\phi_2\right)}\frac{\partial \Delta \Psi\left(\phi_1,\phi_2\right)}{\partial \phi_i},\\
\frac{\partial^2 \zeta_{\mathrm{I}}}{\partial \phi_i \partial \phi_j} &= 2\frac{\zeta_{\mathrm{I}}}{k_{\mathrm{B}}T_0}\frac{\Delta G^*\left(\phi_1,\phi_2\right)}{\Delta \Psi\left(\phi_1,\phi_2\right)}\left[\left(2\frac{\Delta G^*\left(\phi_1,\phi_2\right)}{k_{\mathrm{B}}T_0}-3\right)\frac{1}{\Delta \Psi\left(\phi_1,\phi_2\right)}\frac{\partial \Delta \Psi\left(\phi_1,\phi_2\right)}{\partial \phi_i}\frac{\partial \Delta \Psi\left(\phi_1,\phi_2\right)}{\partial \phi_j}+\frac{\partial^2 \Delta \Psi\left(\phi_1,\phi_2\right)}{\partial \phi_i \partial \phi_j}\right],
\end{aligned} \tag{B.1}$$

where the first derivative of the change in the free energy $\Delta \Psi\left(\phi_1,\phi_2\right)$ is given by

$$\begin{aligned}
\frac{\partial \Delta \Psi\left(\phi_1,\phi_2\right)}{\partial \phi_i} &= (-1)^{i+1} w_{\mathrm{L}} \frac{N_{\mathrm{c0}}}{3} k_{\mathrm{B}} T_0 \kappa n \left[\frac{1}{\left(\phi_i+1\right)}-\frac{\pi}{\sqrt{n}}\cot\left(\frac{\pi}{\sqrt{n}}\left(\phi_i+1\right)\right)\right],\\
\frac{\partial^2 \Delta \Psi\left(\phi_1,\phi_2\right)}{\partial \phi_i \partial \phi_j} &= \begin{cases} (-1)^{i+1} w_{\mathrm{L}} \frac{N_{\mathrm{c0}}}{3} k_{\mathrm{B}} T_0 \kappa n \left[-\frac{1}{\left(\phi_i+1\right)^2}+\frac{\pi^2}{n}\frac{1}{\sin\left(\frac{\pi}{\sqrt{n}}\left(\phi_i+1\right)\right)}\right] & i=j \\ 0 & i\neq j. \end{cases}
\end{aligned} \tag{B.2}$$

With regard to the secondary crystallinity in unloading (i.e. $\Lambda_i^{\mathrm{c\,max}} = \text{const}$), Eq. (5), the first and the second derivatives with respect to nonlocal variables $\{\phi_1, \phi_2\}$ can be expressed by

$$\begin{aligned}
\frac{\partial \zeta_{\mathrm{II}}}{\partial \phi_i} &= 2B_2 \exp\left(-\frac{\Delta\overline{G}^*(\phi_i)}{k_{\mathrm{B}}T_0}\right)\left[\exp\left(-\frac{\Delta\widehat{G}^*\left(\Lambda_i^{\mathrm{c\,max}}-1\right)}{k_{\mathrm{B}}T_0}\right)\frac{\Delta\overline{G}^*(\phi_i)}{k_{\mathrm{B}}T_0}\right.\\
&\left.-\exp\left(-\frac{\Delta\widehat{G}^*(\phi_i)}{k_{\mathrm{B}}T_0}\right)\left(\frac{\Delta\overline{G}^*(\phi_i)}{k_{\mathrm{B}}T_0}+\frac{\Delta\widehat{G}^*(\phi_i)}{k_{\mathrm{B}}T_0}\right)\right]\frac{1}{\Psi_i(\phi_i)}\frac{\partial\Psi_i(\phi_i)}{\partial\phi_i}\\
\frac{\partial^2\zeta_{\mathrm{II}}}{\partial\phi_i\partial\phi_i} &= \left[\frac{1}{\frac{\partial\Psi_i(\phi_i)}{\partial\phi_i}}\frac{\partial^2\Psi(\phi_i)}{\partial\phi_i\partial\phi_i}+\left(2\frac{\Delta\overline{G}^*(\phi_i)}{k_{\mathrm{B}}T_0}-3\right)\frac{1}{\Psi_i(\phi_i)}\frac{\partial\Psi_i(\phi_i)}{\partial\phi_i}\right]\frac{\partial\zeta_{\mathrm{II}}}{\partial\phi_i}\\
&-4B_2\exp\left(-\frac{\Delta\overline{G}^*(\phi_i)}{k_{\mathrm{B}}T_0}-\frac{\Delta\widehat{G}^*(\phi_i)}{k_{\mathrm{B}}T_0}\right)\left(\frac{\Delta\overline{G}^*(\phi_i)}{k_{\mathrm{B}}T_0}+\frac{\Delta\widehat{G}^*(\phi_i)}{k_{\mathrm{B}}T_0}\right)\frac{\Delta\widehat{G}^*(\phi_i)}{k_{\mathrm{B}}T_0}\left(\frac{1}{\Psi_i(\phi_i)}\frac{\partial\Psi_i(\phi_i)}{\partial\phi_i}\right)^2
\end{aligned} \tag{B.3}$$

Appendix C. Derivation of the geometrical stiffness matrix

In order to derive the geometrical tangent stiffness matrix, the product of the modified second Piola–Kirchhoff stress tensor and the linearization of the variation of the modified Green–Lagrange strain tensor, i.e. $\overline{\mathbf{S}} : \Delta\delta\overline{\mathbf{E}}$, is converted to a matrix form. By adopting (90), it can be expressed as follows

$$\begin{aligned}
\bar{\mathbf{S}} : \Delta\delta\overline{\mathbf{E}} &= \frac{1}{2}\left(\frac{\overline{J}}{J}\right)^{2/3}\left(\overline{\mathbf{S}} : \Delta\delta\mathbf{C}\right)+\frac{1}{3}\left[\frac{\delta\overline{J}}{\overline{J}}-\frac{\delta J}{J}\right]\left(\overline{\mathbf{S}} : \Delta\overline{\mathbf{C}}\right)+\frac{1}{3}\left[\frac{\Delta\overline{J}}{\overline{J}}-\frac{\Delta J}{J}\right]\left(\overline{\mathbf{S}} : \delta\overline{\mathbf{C}}\right)\\
&+\frac{1}{3}\left[\frac{\Delta\delta\overline{J}}{\overline{J}}-\frac{\Delta\delta J}{J}-\frac{5}{3}\frac{\delta\overline{J}}{\overline{J}}\frac{\Delta\overline{J}}{\overline{J}}+\frac{1}{3}\frac{\delta J}{J}\frac{\Delta J}{J}+\frac{2}{3}\frac{\delta\overline{J}}{\overline{J}}\frac{\Delta J}{J}+\frac{2}{3}\frac{\delta J}{J}\frac{\Delta\overline{J}}{\overline{J}}\right]\left(\overline{\mathbf{S}} : \overline{\mathbf{C}}\right)
\end{aligned} \tag{C.1}$$

Then, the linearization $\Delta\delta\mathbf{C} = \delta\mathbf{F}^{\mathrm{T}}\Delta\mathbf{F} + \Delta\mathbf{F}^{\mathrm{T}}\delta\mathbf{F}$ is used to derive the matrix form of $\overline{\mathbf{S}} : \Delta\delta\mathbf{C}$ as follows

$$\frac{1}{2}\overline{\mathbf{S}} : \Delta\delta\mathbf{C} = \sum_{I=1}^{N_{en}}\sum_{J=1}^{N_{en}}\left(\sum_{i=1}^{3}\sum_{j=1}^{3}\frac{\partial N_I}{\partial X_i}\overline{S}_{ij}\frac{\partial N_J}{\partial X_j}\right)\delta\underline{\widehat{\boldsymbol{u}}}_e^I\cdot\Delta\underline{\widehat{\boldsymbol{u}}}_e^I = \delta\underline{\widehat{\boldsymbol{U}}}_e^{\mathrm{T}}\underline{\underline{\mathbf{k}}}_G\Delta\underline{\widehat{\boldsymbol{U}}}_e, \tag{C.2}$$

where the matrix $\underline{\underline{\mathbf{k}}}_G$ resembles the geometric stiffness matrix in the standard finite element formulation and it is given by

$$\underline{\underline{\mathbf{k}}}_G = \begin{bmatrix}\underline{\underline{\mathbf{G}}}_{11} & \underline{\underline{\mathbf{G}}}_{12} & \cdots & \underline{\underline{\mathbf{G}}}_{18}\\ \underline{\underline{\mathbf{G}}}_{21} & \underline{\underline{\mathbf{G}}}_{22} & \cdots & \underline{\underline{\mathbf{G}}}_{28}\\ \vdots & \vdots & \ddots & \vdots\\ \underline{\underline{\mathbf{G}}}_{81} & \underline{\underline{\mathbf{G}}}_{82} & \cdots & \underline{\underline{\mathbf{G}}}_{88}\end{bmatrix},\quad \underline{\underline{\mathbf{G}}}_{IJ} = \left(\sum_{i=1}^{3}\sum_{j=1}^{3}\frac{\partial N_I}{\partial X_i}\overline{S}_{ij}\frac{\partial N_J}{\partial X_j}\right)\underline{\underline{\mathbf{I}}}, \tag{C.3}$$

at which $\underline{\underline{\mathbf{I}}}$ is the 3×3 identity matrix. The linearization of the variation of the point-wise volume change can be expressed in the following way

$$\Delta\delta J = \underbrace{\delta\underline{\widehat{\boldsymbol{U}}}_e^{\mathrm{T}}\underline{\underline{\mathbf{G}}}_C\Delta\underline{\widehat{\boldsymbol{U}}}_e}_{J\mathbf{C}^{-1}:\frac{1}{2}\Delta\delta\mathbf{C}} + \underbrace{\delta\underline{\widehat{\boldsymbol{U}}}_e^{\mathrm{T}}\left(\frac{1}{J}\underline{\boldsymbol{a}}_1\underline{\boldsymbol{a}}_1^{\mathrm{T}}\right)\Delta\underline{\widehat{\boldsymbol{U}}}_e}_{\frac{1}{2}\delta\mathbf{C}:\left(J\mathbf{C}^{-1}\otimes\mathbf{C}^{-1}\right):\frac{1}{2}\Delta\mathbf{C}} - \underbrace{\delta\underline{\widehat{\boldsymbol{U}}}_e^{\mathrm{T}}\left(J\underline{\underline{\mathbf{B}}}_u^{\mathrm{T}}\underline{\underline{\mathbf{D}}}_C\underline{\underline{\mathbf{B}}}_u\right)\Delta\underline{\widehat{\boldsymbol{U}}}_e}_{-J\Delta\mathbf{C}^{-1}:\frac{1}{2}\delta\mathbf{C}} = \delta\underline{\widehat{\boldsymbol{U}}}_e^{\mathrm{T}}\underline{\underline{\mathbf{a}}}_2\Delta\underline{\widehat{\boldsymbol{U}}}_e, \tag{C.4}$$

where the matrix $\underline{\underline{\mathbf{a}}}_2$ is defined by

$$\underline{\underline{\mathbf{a}}}_2 = \underline{\underline{\mathbf{G}}}_C + \frac{1}{J}\underline{\boldsymbol{a}}_1\underline{\boldsymbol{a}}_1^{\mathrm{T}} - J\underline{\underline{\mathbf{B}}}_u^{\mathrm{T}}\underline{\underline{\mathbf{D}}}_C\underline{\underline{\mathbf{B}}}_u. \tag{C.5}$$

Also, the matrix $\underline{\underline{\mathbf{G}}}_C$ in (C.5) can be expressed as follows

$$\underline{\underline{\mathbf{G}}}_C = \begin{bmatrix}\underline{\underline{\mathbf{G}}}_{11}^C & \underline{\underline{\mathbf{G}}}_{12}^C & \cdots & \underline{\underline{\mathbf{G}}}_{18}^C\\ \underline{\underline{\mathbf{G}}}_{21}^C & \underline{\underline{\mathbf{G}}}_{22}^C & \cdots & \underline{\underline{\mathbf{G}}}_{28}^C\\ \vdots & \vdots & \ddots & \vdots\\ \underline{\underline{\mathbf{G}}}_{81}^C & \underline{\underline{\mathbf{G}}}_{82}^C & \cdots & \underline{\underline{\mathbf{G}}}_{88}^C\end{bmatrix},\quad \underline{\underline{\mathbf{G}}}_{IJ}^C = \left(\sum_{i=1}^{3}\sum_{j=1}^{3}\frac{\partial N_I}{\partial X_i}C_{ij}^{-1}\frac{\partial N_J}{\partial X_j}\right)\underline{\underline{\mathbf{I}}}, \tag{C.6}$$

and $\underline{\underline{\mathbf{D}}}_C$ is a 6×6 matrix that represents the fourth order tensor $2\left(\mathbf{C}^{-1}\odot\mathbf{C}^{-1}\right)$ in which the operator $\odot$ is a symmetrized tensor product of two second-order tensors defined by

$$(\mathbf{A}\odot\mathbf{B})_{ijkl} = \frac{1}{2}\left(A_{ik}B_{jl}+A_{il}B_{jk}\right). \tag{C.7}$$

Now, $\Delta\delta\overline{J}$ can be re-written as follows

$$\Delta\delta\overline{J} = \delta\underline{\widehat{\boldsymbol{U}}}_e^{\mathrm{T}}\underline{\underline{\bar{\mathbf{a}}}}_2\Delta\underline{\widehat{\boldsymbol{U}}}_e.\quad \underline{\underline{\bar{\mathbf{a}}}}_2 = \frac{1}{\Omega_e^0}\int_{\Omega_e^0}\underline{\underline{\mathbf{a}}}_2\,d\Omega_e^0. \tag{C.8}$$

Finally, using (C.2), (102), (103), (C.4) and (C.8), the multiplication (C.1) can be re-written as

$$\overline{\mathbf{S}} : \Delta\delta\overline{\mathbf{E}} = \delta\hat{\underline{U}}_e^{\mathrm{T}} \overline{\underline{\underline{\mathbf{k}}}}_G \Delta\hat{\underline{U}}_e, \tag{C.9}$$

where $\overline{\underline{\underline{\mathbf{k}}}}_G$ represents the geometric stiffness matrix for the mixed finite element formulation and is given by

$$\begin{aligned}\overline{\underline{\underline{\mathbf{k}}}}_G = &\left(\frac{\overline{J}}{J}\right)^{2/3} \underline{\underline{\mathbf{k}}}_G + \frac{2}{3}\left(\frac{\overline{\underline{\mathbf{a}}}_1}{\overline{J}} - \frac{\underline{\mathbf{a}}_1}{J}\right)\left(\overline{\underline{\mathbf{S}}}^{\mathrm{T}}\overline{\underline{\mathbf{B}}}\right) + \frac{2}{3}\left(\overline{\underline{\underline{\mathbf{B}}}}_u^{\mathrm{T}}\overline{\underline{\mathbf{S}}}\right)\left(\frac{\overline{\underline{\mathbf{a}}}_1}{\overline{J}} - \frac{\underline{\mathbf{a}}_1}{J}\right)^{\mathrm{T}} \\ &+ \frac{\left(\overline{\mathbf{S}} : \overline{\mathbf{C}}\right)}{3}\left[\frac{\overline{\underline{\underline{\mathbf{a}}}}_2}{\overline{J}} - \frac{\underline{\underline{\mathbf{a}}}_2}{J} - \frac{5}{3}\frac{\overline{\underline{\mathbf{a}}}_1\overline{\underline{\mathbf{a}}}_1^{\mathrm{T}}}{\overline{J}^2} + \frac{1}{3}\frac{\underline{\mathbf{a}}_1\underline{\mathbf{a}}_1^{\mathrm{T}}}{J^2} + \frac{2}{3}\frac{\underline{\mathbf{a}}_1\overline{\underline{\mathbf{a}}}_1^{\mathrm{T}}}{J\overline{J}} + \frac{2}{3}\frac{\overline{\underline{\mathbf{a}}}_1\underline{\mathbf{a}}_1^{\mathrm{T}}}{\overline{J}J}\right].\end{aligned} \tag{C.10}$$

Data availability

The source data are publicly available on Zenodo at https://doi.org/10.5281/zenodo.21356943.

References

[1] T.-T. Mai, T. Yasui, R. Tanaka, H. Masunaga, T. Kabe, K. Tsunoda, S. Sakurai, K. Urayama, Unraveling non-uniform strain-induced crystallization near a crack tip in natural rubber, Adv. Sci. 11 (12) (2024) 2307741.

[2] J.R. Samaca Martinez, J.-B. Le Cam, X. Balandraud, E. Toussaint, J. Caillard, Mechanisms of deformation in crystallizable natural rubber. Part 1: Thermal characterization, Polymer 54 (11) (2013) 2717–2726, http://dx.doi.org/10.1016/j.polymer.2013.03.011.

[3] J.-B. Le Cam, Strain-induced crystallization in rubber: A new measurement technique, Strain (October) (2018) e12256.

[4] D. Nozaki, T.-T. Mai, K. Tsunoda, K. Urayama, Tracking the evolution of heterogeneous crystallization driven by complex deformation scenarios in natural rubber, Macromolecules 58 (8) (2025) 4059–4069.

[5] R. Dargazany, V.N. Khiêm, M. Itskov, A generalized network decomposition model for the quasi-static inelastic behavior of filled elastomers, Int. J. Plast. 63 (2014) 94–109, http://dx.doi.org/10.1016/j.ijplas.2013.12.004.

[6] S.J. Mistry, S. Govindjee, A micro-mechanically based continuum model for strain-induced crystallization in natural rubber, Int. J. Solids Struct. 51 (2) (2014) 530–539, http://dx.doi.org/10.1016/j.ijsolstr.2013.10.027.

[7] R. Rastak, C. Linder, A non-affine micro-macro approach to strain-crystallizing rubber-like materials, J. Mech. Phys. Solids 111 (2018) 67–99, http://dx.doi.org/10.1016/j.jmps.2017.10.007.

[8] R. Behnke, T. Berger, M. Kaliske, Numerical modeling of time- and temperature-dependent strain-induced crystallization in rubber, Int. J. Solids Struct. 141–142 (2018) 15–34, http://dx.doi.org/10.1016/j.ijsolstr.2018.01.034.

[9] A. Nateghi, H. Dal, M.-A. Keip, C. Miehe, An affine microsphere approach to modeling strain-induced crystallization in rubbery polymers, Contin. Mech. Thermodyn. 30 (3) (2018) 485–507, http://dx.doi.org/10.1007/s00161-017-0612-8.

[10] A. Gros, B. Huneau, E. Verron, M. Tosaka, A physically-based model for strain-induce d crystallization in natural rubber . Part I : Life cycle of a crystallite, J. Mech. Phys. Solids 125 (2019) 164–177, http://dx.doi.org/10.1016/j.jmps.2018.12.011.

[11] A. Gros, E. Verron, B. Huneau, A physically-base d model for strain-induce d crystallization in natural rubber . Part II : Derivation of the mechanical model, J. Mech. Phys. Solids 125 (2019) 255–275, http://dx.doi.org/10.1016/j.jmps.2018.12.014.

[12] Q. Guo, F. Zaïri, A physically-based thermo-mechanical model for stretch-induced crystallizable rubbers: Crystallization thermodynamics and chain-network crystallization anisotropy, Int. J. Plast. 131 (2020) 102724, http://dx.doi.org/10.1016/j.ijplas.2020.102724.

[13] K. Loos, A.B. Aydogdu, A. Lion, M. Johlitz, J. Calipel, Strain-induced crystallisation in natural rubber : a thermodynamically consistent model of the material behaviour using a multiphase approach, Contin. Mech. Thermodyn. 32 (2) (2020) 501–526, http://dx.doi.org/10.1007/s00161-019-00859-y.

[14] P.K. Arunachala, R. Rastak, C. Linder, Energy based fracture initiation criterion for strain-crystallizing rubber-like materials with pre-existing cracks, J. Mech. Phys. Solids 157 (2021) 104617.

[15] J.R. Samaca Martinez, J.-B. Le Cam, X. Balandraud, E. Toussaint, J. Caillard, Mechanisms of deformation in crystallizable natural rubber. Part 2: Quantitative calorimetric analysis, Polymer 54 (11) (2013) 2727–2736, http://dx.doi.org/10.1016/j.polymer.2013.03.012.

[16] V.N. Khiêm, M. Itskov, Analytical network-averaging of the tube model: Strain-induced crystallization in natural rubber, J. Mech. Phys. Solids 116 (2018) 350–369.

[17] V.N. Khiêm, J.-B. Le Cam, S. Charlès, M. Itskov, Thermodynamics of strain-induced crystallization in filled natural rubber under uni- and biaxial loadings. Part II: Physically-based constitutive theory, J. Mech. Phys. Solids 159 (2022) 104712, http://dx.doi.org/10.1016/j.jmps.2021.104712.

[18] J.L. Ericksen, Equilibrium of bars, J. Elasticity 5 (1975) 191–201.

[19] D. Schryvers, L. Toth, Y. Ma, L. Tanner, Nucleation and growth of the Ni5Al3 phase in Ni-Al austenite and martensite, Le J. de Phys. IV 5 (C2) (1995) C2–299.

[20] D. Huang, X. Ran, Y. Cai, X. Liu, L. Lu, Strain partitioning in dual-phase eutectic high-entropy alloy: Dependence on phase boundary morphology, Scr. Mater. 247 (2024) 116077.

[21] J.-B. Le Cam, A. Tayeb, S. Charlè, First evidence and characterization of strain-induced crystallization heterogeneity in natural rubber under homogeneous strain states, Polymer 255 (2022) 125120.

[22] B.D. Coleman, Necking and drawing in polymeric fibers under tension, Arch. Ration. Mech. Anal. 83 (1983) 115–137.

[23] G. Barsch, J. Krumhansl, Twin boundaries in ferroelastic media without interface dislocations, Phys. Rev. Lett. 53 (11) (1984) 1069.

[24] E.C. Aifantis, On the microstructural origin of certain inelastic models, J. Eng. Mater. Technol. 106 (1984) 326–330.

[25] G. Pijaudier-Cabot, Z. Bažant, Nonlocal damage theory, J. Eng. Mech. 113 (10) (1988) 1512–1533.

[26] R.H. Peerlings, R. De Borst, W.A. Brekelmans, J.H. De Vree, Gradient enhanced damage for quasi-brittle materials, Internat. J. Numer. Methods Engrg. 39 (19) (1996) 3391–3403, http://dx.doi.org/10.1002/(SICI)1097-0207(19961015)39:19<3391::AID-NME7>3.0.CO;2-D.

[27] N. Fleck, J. Hutchinson, in: J.W. Hutchinson, T.Y. Wu (Eds.), Strain Gradient Plasticity, in: Advances in Applied Mechanics, vol. 33, Elsevier, 1997, pp. 295–361.

[28] M. Ortiz, E. Repetto, Nonconvex energy minimization and dislocation structures in ductile single crystals, J. Mech. Phys. Solids 47 (2) (1999) 397–462.

[29] X. Ren, L. Truskinovsky, Finite scale microstructures in nonlocal elasticity, J. Elast. Phys. Sci. Solids 59 (1) (2000) 319–355.

[30] Q.-S. Nguyen, S. Andrieux, The non-local generalized standard approach: a consistent gradient theory, Comptes Rendus Mécanique 333 (2) (2005) 139–145.

[31] S. Forest, Micromorphic approach for gradient elasticity, viscoplasticity, and damage, J. Eng. Mech. 135 (3) (2009) 117–131.

[32] C. Kuhn, R. Müller, A continuum phase field model for fracture, Eng. Fract. Mech. 77 (18) (2010) 3625–3634.
[33] G. Del Piero, A variational approach to fracture and other inelastic phenomena, J. Elasticity 112 (2013) 3–77.
[34] A. Bertram, S. Forest, The thermodynamics of gradient elastoplasticity, Contin. Mech. Thermodyn. 26 (2014) 269–286.
[35] M. Ambati, T. Gerasimov, L. De Lorenzis, Phase-field modeling of ductile fracture, Comput. Mech. 55 (2015) 1017–1040.
[36] F. Cazes, N. Moës, Comparison of a phase-field model and of a thick level set model for brittle and quasi-brittle fracture, Internat. J. Numer. Methods Engrg. 103 (2) (2015) 114–143.
[37] C. Miehe, F. Welschinger, M. Hofacker, Thermodynamically consistent phase-field models of fracture: Variational principles and multi-field FE implementations, Internat. J. Numer. Methods Engrg. 83 (10) (2010) 1273–1311, http://dx.doi.org/10.1002/nme.
[38] V.N. Khiêm, M. Jabareen, R. Poudel, X. Tang, M. Itskov, Modeling of textile composite using analytical network-averaging and gradient damage approach, J. Mech. Phys. Solids 193 (2024) 105874.
[39] A. Gros, M. Tosaka, B. Huneau, E. Verron, S. Poompradub, K. Senoo, Dominating factor of strain-induced crystallization in natural rubber, Polymer 76 (2015) 230–236, http://dx.doi.org/10.1016/j.polymer.2015.08.058.
[40] V.N. Khiêm, M. Itskov, Analytical network-averaging of the tube model: Rubber elasticity, J. Mech. Phys. Solids 95 (2016) 254–269, http://dx.doi.org/10.1016/j.jmps.2016.05.030.
[41] V.N. Khiêm, M. Itskov, An averaging based tube model for deformation induced anisotropic stress softening of filled elastomers, Int. J. Plast. 90 (2017) 96–115, http://dx.doi.org/10.1016/j.ijplas.2016.12.007.
[42] V.N. Khiêm, M. Itskov, Analytical network-averaging of the tube model: Mechanically induced chemiluminescence in elastomers, Int. J. Plast. 102 (2018) 1–15, http://dx.doi.org/10.1016/j.ijplas.2017.11.001.
[43] S. Toki, I. Sics, S. Ran, L. Liu, B.S. Hsiao, S. Murakami, K. Senoo, S. Kohjiya, New insights into structural development in natural rubber during uniaxial deformation by in situ synchrotron X-ray diffraction, Macromolecules 35 (17) (2002) 6578–6584, http://dx.doi.org/10.1021/ma0205921.
[44] S. Murakami, K. Senoo, S. Toki, S. Kohjiya, Structural development of natural rubber during uniaxial stretching by in situ wide angle X-ray diffraction using a synchrotron radiation, Polymer 43 (7) (2002) 2117–2120, http://dx.doi.org/10.1016/S0032-3861(01)00794-7.
[45] R. Ortigosa, A.J. Gil, A new framework for large strain electromechanics based on convex multi-variable strain energies: Finite element discretisation and computational implementation, Comput. Methods Appl. Mech. Engrg. 302 (2016) 329–360.
[46] R. Poya, A.J. Gil, R. Ortigosa, R. Sevilla, J. Bonet, W.A. Wall, A curvilinear high order finite element framework for electromechanics: From linearised electro-elasticity to massively deformable dielectric elastomers, Comput. Methods Appl. Mech. Engrg. 329 (2018) 75–117.
[47] D. Bishara, M. Jabareen, A reduced mixed finite-element formulation for modeling the viscoelastic response of electro-active polymers at finite deformation, Math. Mech. Solids 24 (5) (2019) 1578–1610.
[48] M. Horák, A.J. Gil, R. Ortigosa, M. Kružík, A polyconvex transversely-isotropic invariant-based formulation for electro-mechanics: Stability, minimisers and computational implementation, Comput. Methods Appl. Mech. Engrg. 403 (2023) 115695, http://dx.doi.org/10.1016/j.cma.2022.115695, URL: https://www.sciencedirect.com/science/article/pii/S0045782522006508.
[49] R. Ogden, Non-Linear Elastic Deformations, Dover Publications, 1997.
[50] K.Y. Volokh, Loss of ellipticity in elasticity with energy limiters, Eur. J. Mech. A Solids 63 (2017) 36–42, http://dx.doi.org/10.1016/j.euromechsol.2016.10.003.
[51] D.J. Griffiths, Introduction to Electrodynamics, fourth ed., Pearson, 2013.
[52] W. Kuhn, H. Kuhn, Statistische und energieelastische rückstellkraft bei stark auf dehnung beanspruchten fadenmolekeln, Helv. Chim. Acta 29 (5) (1946) 1095–1115.
[53] V.N. Khiêm, A.J. Gil, Systematic general inelasticity, 2026, submitted for publication.
[54] B.D. Coleman, W. Noll, The thermodynamics of elastic materials with heat conduction and viscosity, Arch. Ration. Mech. Anal. 13 (1) (1963) 167–178, http://dx.doi.org/10.1007/BF01262690.
[55] R. de Borst, C.V. Verhoosel, Gradient damage vs. phase-field approaches for fracture: Similarities and differences, Comput. Methods Appl. Mech. Engrg. 312 (2016) 78–94, http://dx.doi.org/10.1016/j.cma.2016.05.015.
[56] Dassault Systèmes Simulia Corp., ABAQUS Analysis User's Guide, Providence, RI, USA, 2022.
[57] X. Chen, L. Meng, W. Zhang, K. Ye, C. Xie, D. Wang, W. Chen, M. Nan, S. Wang, L. Li, Frustrating strain-induced crystallization of natural rubber with biaxial stretch, ACS Appl. Mater. & Interfaces 11 (50) (2019) 47535–47544.
[58] P. Rosendahl, M. Drass, J. Felger, J. Schneider, W. Becker, Equivalent strain failure criterion for multiaxially loaded incompressible hyperelastic elastomers, Int. J. Solids Struct. 166 (2019) 32–46.
[59] J. Zhu, S. Liu, Y. Lu, H. Cheng, X. Han, L. Liu, L. Meng, W. Yu, K. Cui, L. Li, A versatile biaxial stretching device for in situ synchrotron radiation small-and wide-angle x-ray scattering measurements of polymer films, Rev. Sci. Instrum. 94 (2) (2023).
[60] A. Chrysochoos, Analyse du comportement des matériaux par thermographie Infra Rouge, in: Colloque Photomécanique, Vol. 95, 1995, pp. 201–211.
[61] B. Berthel, A. Chrysochoos, B. Wattrisse, A. Galtier, Infrared image processing for the calorimetric analysis of fatigue phenomena, Exp. Mech. 48 (2008) 79–90.
[62] V.N. Khiêm, J.-B. Le Cam, S. Charlès, M. Itskov, Thermodynamics of strain-induced crystallization in filled natural rubber under uni- and biaxial loadings, Part I: Complete energetic characterization and crystallinity evaluation, J. Mech. Phys. Solids 159 (2022) 104701, http://dx.doi.org/10.1016/j.jmps.2021.104701.